UNIVERSITY OF HELSINKI REPORT SERIES IN PHYSICS

HU-P-D83

ADVANCED EXPERIMENTAL METHODS IN COMPTON SCATTERING SPECTROSCOPY

Jarkko K. Laukkanen

X-Ray Laboratory
Department of Physics
Faculty of Science
University of Helsinki
Helsinki, Finland

ACADEMIC DISSERTATION

To be presented, with the permission of
the Faculty of Science of the University of Helsinki,
for public criticism in Auditorium F-I of
the Department of Physics on 17th June 2000, at 12 o'clock.

Helsinki 2000

ISBN 951-45-8199-7 (nid.)
ISBN 952-91-2308-6 (PDF)
ISSN 0356-0961
Helsingin yliopiston verkkojulkaisut
Helsinki 2000

Preface

This thesis is based on research done at the X-Ray Laboratory of the Department of Physics (University of Helsinki, Finland), and at the beamline ID15B of the European Synchrotron Radiation Facility (Grenoble, France), both of which are acknowledged.

First, I wish to thank Professors Timo Paakkari and Juhani Keinonen for providing the opportunity to work at the X-Ray Laboratory and at the Department of Physics. The staff of the ID15B is acknowledged for collaboration and support during the experiments done there, and all the co-authors of the papers published, and of those to be published, are acknowledged for fruitful co-operation.

Further, I wish to thank my supervisors, Professor Seppo Manninen and Doctor Keijo Hämäläinen. You introduced me to the world of inelastic X-ray scattering, and you taught me the essentials of science. My work is partly built on your knowledge, experience and expertise. Thank you for your generous support and trust on my abilities.

Moreover, I wish to thank the staff of the X-Ray Laboratory. You have created a nice, encouraging and inspiring work atmosphere. It has been, and will be, a pleasure to know you and to work with you. Yet, you have taught me that not every experiment works as expected. Some might work out better. Both the physicist and the engineer sides of mind are needed for success. Special thanks to Dr. Merja Blomberg, M.Sc. Simo Huotari and M.Sc. Heikki Sutinen.

Finally, I wish to thank my parents, brothers and friends. Without your genuine love, care, support and patience I would not be here now. You have been irreplaceable in providing the balancing acts between my work and the rest of life, both of which have been a lot more rewarding thanks to you.

M.A. Krista Kindt-Sarojärvi is acknowledged for proof-reading this thesis. Financial support, both from the Academy of Finland and the National Science Foundation (USA), is gratefully acknowledged.

Helsinki, 31st March 2000

Jarkko K. Laukkanen

J. K. Laukkanen: Advanced Experimental Methods in Compton Scattering Spectroscopy, University of Helsinki (2000), 61 pages + Appendices, University of Helsinki, Report Series in Physics, HU-P-D83, ISSN 0356-0961, ISBN 951-45-8199-7.

Classification (INSPEC): 07.85.Nc, 07.85.Qe, 78.70.Ck
Keywords: Inelastic X-Ray Scattering, Synchrotron Radiation, Experimental Methods

Abstract

The Compton scattering technique, i.e. inelastic X-ray scattering spectroscopy at large energy and momentum transfers, was used to study the ground-state electronic properties of several condensed matter systems. In addition, the limits for the applicability of the technique for the inner-shell electrons at intermediate energy and momentum transfers has been tested. Both a conventional radiation source based on a X-ray tube, and a modern third generation synchrotron radiation source were utilized for the experiments.

First, binary aluminum transition-metal alloys were studied to test the validity of a very recently developed theoretical and computational scheme. The model was shown to explain successfully the Fermi surface related features found experimentally. Secondly, the validity of the impulse approximation was tested on two distinguishably different radiation sources using the coincidence technique. On a conventional source, both the shape of the core-shell profile and its absolute cross-section were extracted for the first time with an accuracy good enough for a direct quantitative comparison with theory. The deviations found between the experiment and the theoretical calculations done within the bounds of the impulse approximation are explained by the more advanced quantum-mechanical calculations. For the experiment done on a synchrotron source, a new scheme for the optimization of the experimental parameters was developed which enabled to reach the same level in the true-to-chance coincidence ratio as before only with conventional sources. Thirdly, electron correlation effects were studied in a high-pressure experiment on sodium. The free electron density was varied directly by changing the high pressure applied to the sample. The effects of the electron correlation to the Compton profile were demonstrated. Finally, the electronic properties of a high-T_C superconductor $La_{1.85}Sr_{0.15}CuO_4$ and a decagonal quasicrystal $Al_{0.72}Co_{0.17}Ni_{0.11}$, a ternary aluminum transition-metal alloy, were studied. The theoretical calculations for the superconductor were done for the undoped La_2CuO_4 using the KKR-methodology. Due to the practical difficulties in modeling of a non-periodic system, no exact theoretical model exists yet for the quasicrystals. However, an anisotropy in the electronic momentum density was discovered for the first time, and the development of a computational scheme applicable to quasicrystals is in progress.

Contents

List of Papers

This thesis consists of an introductory part for the four already published research papers, sorted in chronological order and referred to by the Roman numerals **I** – **IV** in the text, and of two new reports (Sections 6.1 and 6.2) on yet unpublished results.

I: Seppo Manninen, Veijo Honkimäki, Keijo Hämäläinen, Jarkko Laukkanen, Claudia Blaas, Joseph Redinger, Joanne McCarthy and Pekka Suortti: *Compton scattering study of the electronic properties of the transition-metal alloys FeAl, CoAl, and NiAl*
Phys. Rev. B **53** (1996) 7714 – 7720

II: Jarkko Laukkanen, Keijo Hämäläinen and Seppo Manninen: *The absolute double-differential Compton scattering cross-section of Cu 1s electrons*
J. Phys.: Condens. Matter **8** (1996) 2153 – 2162

III: Jarkko Laukkanen, Keijo Hämäläinen, Seppo Manninen and Veijo Honkimäki: *Inelastic X-ray scattering study on Ag K-shell electrons utilizing coincidence technique on a synchrotron radiation source*
Nucl. Instr. and Meth. A **416** (1998) 475 – 484

IV: Simo Huotari, Keijo Hämäläinen, Jarkko Laukkanen, Aleksi Soininen, Seppo Manninen, Chi-Chang Kao, Thomas Buslaps, Mohammad Mezouar and Ho-Kwang Mao: *High pressure Compton scattering*
Recent Advances in High Pressure Science and Technology (In press)

1 Introduction

Inelastic X-ray scattering, discovered by the late Sir A. H. Compton in 1921 [1], has proved its power as an sensitive probe for the ground-state electronic properties of condensed matter systems [2,3]. Also known as Compton scattering, it regained considerable experimental interest in the 1970's when the solid-state detectors became widely available. At the same time, the experimental accuracy reached a level where the precision of the underlying approximations widely used in the basic formulation of the theory of inelastic X-ray scattering became for the first time seriously questioned.

During the recent decade or two, the advances in computing, both in methods and raw processing power, and in experimental techniques, most notable due to the application of synchrotron radiation, have revolutionized the entire field of condensed matter science. The 'old' experiments can be done at a drastically improved performance level, and even some entirely new techniques have emerged to utilize the extraordinary properties of synchrotron radiation, e.g. collimation and polarization [4]. Simultaneously, several other branches of science, for example medicine, life sciences and biology, have started to utilize synchrotron radiation. Further, the developments in theoretical methods have established a serious need for accurate experimental results to check the validity of the models.

The advances have strengthened our understanding of the electronic behavior of the condensed matter systems. Yet, some notable obstacles remain. The high-T_C superconductivity discovered in 1986 [5] and the quasicrystalline solids found in 1984 [6,7] still resist complete understanding of their properties. Partly, this is due to the lack of accurate results obtained with direct-probing experimental techniques, that is, the techniques probing the initial or final states of the electrons directly, e.g. inelastic X-ray scattering, or positron-annihilation. Further, the theoretical models are still in a somewhat unmature state. In the case of the quasicrystals, no exact theory exists to interprete the electronic behavior in terms of the electronic structure due to the restrictions in modeling a quasiperiodic system.

This thesis involves the applications of inelastic X-ray scattering to study several interesting issues in this field, and developments in the experimental techniques to further aid to improve its accuracy and level of applicability in condensed matter research. As a summary, the key results were made feasible either by adopting high-resolution experimental apparatus, e.g. a scanning crystal spectrometer at a third generation synchrotron source, or by taking the performance of an existing measurement technique to a more advanced level, e.g. the coincidence experiments. The advances gained enabled to reach some new experimental results.

The unit system adopted in this thesis is the one most often used in the experimental work in the field of inelastic X-ray scattering. Energy is measured in keV, and momentum in a.u..

2 Inelastic X-Ray Scattering

The theory of inelastic (incoherent) X-ray scattering (IXS) is based on the relativistic treatment of the interactions between electromagnetic radiation at X-ray energies, and quasi-free electrons [8–12]. The underlying foundations together with the most important approximations are reviewed shortly for the intent of understanding IXS from the experimental point of view. Additionally, some of the key characteristics of the IXS process in terms of the experiments are considered.

2.1 Kinematics

The relativistic energy and momentum of the incident and scattered photon ($\hbar\omega_{1,2}$ and $\hbar\mathbf{k}_{1,2}$, respectively), and the initially bound-state but escaped electron ($\sqrt{(m_e c^2)^2 + (c\mathbf{p}_{1,2})^2}$ and $\mathbf{p}_{1,2}$, respectively) conserve in the IXS process. Further, the scattered photon transfers energy $\Delta\big(\hbar\omega\big)$ and momentum $\hbar\,|\mathbf{q}|$ (2.1) to the target electron in the process

$$\hbar\,|\mathbf{q}| = \frac{1}{c}\sqrt{\big(\hbar\omega_1\big)^2 + \big(\hbar\omega_2\big)^2 - 2\,\hbar\omega_1\,\hbar\omega_2\,\cos\varphi}\;, \tag{2.1}$$

where the scattering vector $\mathbf{q} = \mathbf{k}_1$ - $\mathbf{k}_2$, and φ is the scattering angle i.e. the angle between $\mathbf{k}_1$ and $\mathbf{k}_2$. In the non-relativistic context ($\hbar\omega_1 \ll m_e c^2$), the energy transfer $\Delta\big(\hbar\omega\big)$ simplifies to (2.2)

$$\Delta\big(\hbar\omega\big) = \frac{\big(\hbar\mathbf{q}\big)^2}{2m_e} + \frac{\hbar}{m_e}\big(\mathbf{p}_1\cdot\mathbf{q}\big)\;. \tag{2.2}$$

The non-relativistic energy transfer (2.2) consists of two terms, frequently called the recoil-term and the Doppler-term. The recoil-term (the first in (2.2)) describes the kinematics of the IXS process. It depends on the experimental parameters only, defining a mean value of energy transfer (the Compton shift), to which the Doppler-term (the second in (2.2)), dependent on the initial state of the electron at the moment of a scattering event, adds dynamics: the broadening of the line spectrum of inelastically scattered X-rays (the Compton profile) due to the non-zero initial momentum $\mathbf{p}_1$ of the target electron. The IXS process occurs only if the energy transfer (2.2) is greater than the binding energy E_B of the target electron. The IXS process has been denominated to the Compton effect according to its discoverer, Sir A. H. Compton [1].

The scattering vector $\mathbf{q}$ (2.1) offers a convenient base for a coordinate system in order to describe the physics of the IXS process. The component of the target electron's initial momentum $\mathbf{p}_1$ along the scattering vector $\mathbf{q}$, i.e. p_z (2.3) [13], is

$$p_z \;=\; \frac{q}{2} \;-\; \frac{1}{\hbar c}\left(\hbar\omega_1 - \hbar\omega_2\right)\sqrt{\frac{1}{4} + \frac{\left(m_e c^2\right)^2}{2\,\hbar\omega_1\,\hbar\omega_2\left(1-\cos\varphi\right)}}\;. \tag{2.3}$$

The origin of the p_z-scale (in the scattered energy $\hbar\omega_2$) lies below the elastic line, lowered by the energy corresponding to the Compton shift. In the experimental work, p_z is customarily given in atomic units, i.e. multiplied by the Bohr radius a_0.

2.2 Regimes

The various physical phenomena existing within the concept of IXS can be classified in a meaningful way according to the associated energy and momentum transfers relative to the characteristic energies or structural dimensions. The physics is still the same but the phenomena are quite diverse in detail. The three distinct IXS regimes are:

The Compton Scattering Regime ($\Delta\left(\hbar\omega\right) \gg E_B$, $qa_{nl} \gg 1$)

The energy (momentum) transfer is large compared to the binding energy (inverse of the orbital radius a_{nl}) of the target electron. After the scattering process the electron is in a continuum state, not exerting influence to the state of the parent atom, nor to the band structure of the electronic system. The purely atomic excited states which are created decay locally, e.g. by emitting characteristic fluorescence radiation. In experiments with hard X-rays, the large transfer conditions are typically true for a clear majority of the electrons. In most cases, only the innermost shells fail to fulfill this approximation, dangling into the next regime.

The Characteristic Excitation Regime ($\Delta\left(\hbar\omega\right) \simeq E_B$, $qa_{nl} \simeq 1$, or $qa_C \simeq 1$)

The energy (momentum) transfer is comparable to the binding energy (inverse of the orbital radius a_{nl}, or the inter-atomic distances a_C) of the target system. In the IXS spectrum, resonant structures sensitive to the local electronic environment are found, especially near the absorption edges, hence the regime is frequently called the dynamic structure factor regime. Additionally, (resonant) Raman scattering is included in this regime. However, the final state is a non-continuum state but it may also be of a vibrational or rotational type in addition to an electronic one. In some contexts, this regime is customarily called the intermediate momentum transfer region.

The Collective Scattering Regime ($\Delta(\hbar\omega) \ll 1$ keV, $qa_C \ll 1$)

The energy (momentum) transfer is very small compared to the binding energies (inverses of the inter-atomic distances) of the target system. The excitations may be either of a local or collective type. Quite typically, plasmons or phonons are created, enabling studies on the collective dynamics of the electronic system as one entity [14]. Sometimes, this regime is also called the valence electron scattering regime.

2.3 Scattering Cross-Section

The physical quantity determined in an IXS experiment is the strength of the interaction, i.e. the cross-section of the scattering process. Restricted to the non-relativistic scheme, the total Hamiltonian H_{IXS} (2.4) describing the interaction of photons with electrons consists of three parts

$$H_{IXS} = H\big(\hbar\omega\big) \,+\, H\big(\mathbf{p}, V(\mathbf{r})\big) \,+\, H\big(\mathbf{A}\big) \;. \tag{2.4}$$

The photon Hamiltonian $H\big(\hbar\omega\big)$ (2.5) describes the incident photon, specified by its momentum $\mathbf{k}$ and polarization state $\mathbf{e}$, as a quantized electromagnetic field with the aid of the creation and annihilation operators $a^{\dagger}_{\mathbf{k},\mathbf{e}}$ and $a_{\mathbf{k},\mathbf{e}}$, respectively,

$$H\big(\hbar\omega\big) = \sum_{\mathbf{k},\mathbf{e}} \hbar\omega_{\mathbf{k}} \left(a^{\dagger}_{\mathbf{k},\mathbf{e}} a_{\mathbf{k},\mathbf{e}} \,+\, \frac{1}{2}\right) . \tag{2.5}$$

The one-electron Hamiltonian $H\big(\mathbf{p}, V(\mathbf{r})\big)$ (2.6), i.e. the electron in a potential $V(\mathbf{r})$, is specified with the momentum $\mathbf{p}$ of the electron

$$H\big(\mathbf{p}, V(\mathbf{r})\big) = \frac{\mathbf{p}^2}{2m_e} \,+\, V(\mathbf{r}) \;. \tag{2.6}$$

The interaction Hamiltonian $H\big(\boldsymbol{A}\big)$ (2.7) includes the interaction processes of the electromagnetic vector field $\boldsymbol{A}$ with the electron and its spin $\boldsymbol{\sigma}$

$$H\big(\mathbf{A}\big) = \frac{e^2}{2m_e c}\,\mathbf{A}\cdot\mathbf{A} \,+\, \frac{e}{m_e c}\,\mathbf{p}\cdot\mathbf{A} \,+\, \frac{e\hbar}{2m_e c}\,\boldsymbol{\sigma}\cdot\nabla\times\mathbf{A} \;. \tag{2.7}$$

The double-differential IXS cross-section $\left(d^2\sigma/d\hbar\omega_2\, d\Omega_2\right)_{IXS}$ is obtained by following the established methods. The resulting expression is the so-called generalized Kramers-Heisenberg formula (2.8) [15] (the spin-term is omitted here for clarity)

$$\left(\frac{d^2\sigma}{d\hbar\omega_2\, d\Omega_2}\right)_{IXS} = r_0^2\,\frac{\hbar\omega_2}{\hbar\omega_1}\left|\left\langle F\left|e^{(i\mathbf{q}\cdot\mathbf{r})}\right|I\right\rangle\left(\mathbf{e}_1\cdot\mathbf{e}_2^*\right)\right. \tag{2.8}$$

$$-\ \frac{1}{m_e c^2}\sum_N\left(\frac{\left\langle F\left|e^{(i\mathbf{k}_1\cdot\mathbf{r})}(\mathbf{e}_1\cdot\mathbf{p})\right|N\right\rangle\left\langle N\left|e^{(-i\mathbf{k}_2\cdot\mathbf{r})}(\mathbf{e}_2^*\cdot\mathbf{p})\right|I\right\rangle}{E_N - E_I + \hbar\omega_2}\right.$$

$$\left.+\ \frac{\left\langle F\left|e^{(-i\mathbf{k}_2\cdot\mathbf{r})}(\mathbf{e}_2^*\cdot\mathbf{p})\right|N\right\rangle\left\langle N\left|e^{(i\mathbf{k}_1\cdot\mathbf{r})}(\mathbf{e}_1\cdot\mathbf{p})\right|I\right\rangle}{E_N - E_I + \hbar\omega_1 - i\frac{\Gamma_N}{2}}\right)\Bigg|^2$$

$$\times\ \delta\big(\hbar\omega_1 - \hbar\omega_2 + E_I - E_F\big)\ ,$$

where r_0 is the classical electron radius and Γ_N is the energy width of the intermediate state due to its finite life-time. The capitals I, N, F denote the initial, intermediate and final states, respectively.

The first, non-resonant term in (2.8) arises from the $\mathbf{A}\cdot\mathbf{A}$-term in (2.7). In gives both the classic Thomson [16] and Klein-Nishina [17] cross-sections for the elastic ($\hbar\omega_2 = \hbar\omega_1$ and $\big|F\big\rangle = \big|I\big\rangle$) and the inelastic ($\hbar\omega_2 \leq \hbar\omega_1$, $\big|F\big\rangle \neq \big|I\big\rangle$) scattering processes, respectively. The second and third terms in (2.8) both arise from the $\mathbf{p}\cdot\mathbf{A}$-term in (2.7). However, an intermediate $\big|N\big\rangle$ is involved. Further, the last term may behave resonantly, giving rise to quite different processes [18]. For instance, for $\hbar\omega_1 \gtrsim E_B$ the classic photoabsorption occurs. For $\hbar\omega_1 - E_B \sim 0$, the resonant Raman process can contribute significantly to the IXS cross-section.

The importance of the $\mathbf{p}\cdot\mathbf{A}$-term in IXS is not yet a fully settled issue because the first term in (2.8) is the dominant in an IXS process. Yet, both the non-resonant [19] and resonant [20] Raman processes have been observed at X-ray energies and the resonant part was explained theoretically quite quickly [21]. The resonant IXS process occurring in the X-ray range is sometimes called resonant Compton scattering [22] or Raman-Compton scattering [23]. Even the role of coherence effects in the IXS spectra has been assessed [24]. Nevertheless, the importance of both a specific energy and momentum transfer in the scattering process for the given details in the IXS spectra is evident.

2.4 Impulse Approximation

Under typical experimental conditions in IXS experiments, the energy and momentum transfers to most of the electrons, especially to the outer electrons which are of the greatest interest, are large. Thus, the interaction can be considered to take place instantaneously, or impulsively. The rest of the electronic system does not react to the process by relaxing to the new state until the target electron has escaped. Consequently, the potential $V(\mathbf{r})$ is constant from the ejected electron's point of view. However, the potential energy of the electron can not be neglected completely due to the requirement of sufficient energy transfer (2.2) to overcome the E_B in the process, but in the calculations done within the bounds specified above the potential does cancel out [25]. The electron's binding is included insofar as its initial momentum distribution $\mathbf{p}_1$ is concerned.

This condition, also known as the impulse approximation, leads to a very simple expression for the IXS cross-section (2.9) where the experimental factors are separated from the electronic properties of the target

$$\Big(\frac{d^2\sigma}{d\hbar\omega_2\, d\Omega_2}\Big)_{IXS} = \sum_{nl} X\big(\hbar\omega_1, \hbar\omega_2, \varphi\big)\, J_{nl}\big(p_z\big)\ , \tag{2.9}$$

where $X\big(\hbar\omega_1, \hbar\omega_2, \varphi\big)$ is a conversion factor depending on the experimental parameters, and the Compton profile $J_{nl}\big(p_z\big)$ (2.10) of the electron, specified with the quantum numbers n and l, is

$$J_{nl}\big(p_z\big) = \int\limits_{p_x}\int\limits_{p_y} \rho_{nl}\big(\mathbf{p}_1\big)\, dp_x\, dp_y\ , \tag{2.10}$$

where $\rho_{nl}\big(\mathbf{p}_1\big)$ is the initial momentum density of the target electron. The Compton profile $J_{nl}\big(p_z\big)$ is a direct measure of the integrated (in the plane perpendicular to p_z) 3D electronic momentum density $\rho_{nl}\big(\mathbf{p}_1\big)$ projected onto p_z. Further, the full Compton profile is produced simply by summing up the individual electronic profiles. Several schemes to determine the factor $X\big(\hbar\omega_1, \hbar\omega_2, \varphi\big)$ within the framework of the impulse approximation have been published [13,26,27] in order to convert both the experimental profiles to the p_z-scale, and the theoretical ones to the doubly-differential cross-sections.

When applied to deeply-bound electrons, the impulse approximation leads to the so-called infrared divergence of the IXS cross-section in the limit $\hbar\omega_2 \to 0$ [28]. Experimentally, its existence is still quite controversial [23,29–31] [**Paper II**], mainly due to the problems in subtracting the Bremsstrahlung (Section 4.3.1) contribution emitted by the decelerating electrons in the target in a reliable way.

No rigorous physical proof nor justification for the impulse approximation exists despite the fact that both the numerous experiments and the modern quantum-mechanical calculations [32] clearly show that it does work extremely well in the large transfer regime. One good indication of the situation is that there is no consensus on the effects resulting from the failure of the impulse approximation [32–34]. According to some alternative theoretical treatments [35], the correlation between the ejected electron and those remaining in the ionized atom should be incorporated, a feature which is not exclusively implied by the modern quantum-mechanical treatments [32]. However, the recent experimental results indicate a strong support for this view [36].

The Compton profile is strictly symmetric in p_z within the impulse approximation, with the peak of the profile residing at $p_z = 0$. However, several experiments (e.g. on low-Z targets) clearly show appreciable deviations from this picture [37–40]. The peak of the atomic Compton profile is shifted in the $\hbar\omega_2$-scale (the direction of the shift depends on which is the outermost electron shell) and the profiles are clearly asymmetric. Among the several schemes to explain these Compton defects the most widely used approaches are the operator series-expansion methods [41–43], and the evaluation of the $X\big(\hbar\omega_1, \hbar\omega_2, \varphi\big)$-factor in higher orders [44].

2.5 Compton Scattering

After the experimental discovery and the theoretical explanation of the IXS process [1], it was quickly suggested that it could act as a probe for the electronic properties of the target system [45]. During the intervening years, the Compton scattering technique has proved its usefulness as a sensitive probe for the electronic ground-state properties of numerous condensed matter systems [2,3,46–49] (Section 5). First, the utilization of solid-state detectors since the 1970's, and subsequently the employment of high-resolution crystal spectrometers on the modern synchrotron radiation sources (Section 3) since the 1980's have revived the field [3,47–49].

The Compton scattering technique is most sensitive to the spatially extended valence electron states as their contribution is confined to the peak area of the Compton profile due to the lower average momentum. Depending on the energy transfer (2.2), the inner shells might not even participate in the IXS process. Additionally, the interpretation of the acquired Compton spectrum is rather straightforward due to the direct projective character of the process (Section 2.4) although some details are lost because of the same reason.

The 1D Fourier transform of the directional Compton profiles (acquired with p_z along to a given crystal direction) does not give any direct structural information of the target in a general case [50]. Yet, a definite correlation between the electronic structure and the features found in the profiles, or their anisotropies, does exist [51–54]. The anisotropies are taken by subtracting the given directional profiles.

The contributions from the isotropic core states and any residual background are subtracted out. What remains is dominated by the electron wave function phase coherence among the neighboring atoms. However, due to the projective character of the process, small shifts from the actual physical features can occur, e.g. due to misalignment.

The other experimental methods directly probing the electronic properties of matter, e.g. the positron-annihilation technique [55], (polarization dependent) X-ray absorption spectroscopy, X-ray fluorescence spectroscopy, and the various electron spectroscopy techniques [56] each have their pertinent strengths and weaknesses over the Compton scattering technique. They are essentially surface-sensitive techniques, or restricted to relatively thin samples of the order of 0.1 – 10 μm. The high-energy X-rays, on the contrary, typically penetrate mm's or even up to cm's, probing the very bulk of the target. The Compton scattering technique is also quite insensitive to the crystal quality, unlike the methods utilizing electrons or positrons. Even a crystal consisting of crystallites or grains can be considered as 'single' if the mosaic spread in the preferred orientation is less than a few degrees or less than the angular resolution of the spectrometer, whichever is lower.

The various X-ray absorption and fluorescescence techniques are, however, superior to IXS spectroscopy in some respect although the ground-state properties are inaccessible. They probe the chosen electron states, with added capability to selectively utilize resonance and polarization sensitivity to enhance the detection of a given feature. Further, the 2D-ACAR (2D angular correlation of the annihilation radiation) technique can be viewed as a complementary tool to IXS spectroscopy. It gives the 2D projection of the 3D electronic momentum density along the direction perpendicular to the detector plane, while in IXS spectroscopy the momentum density integrated over the plane perpendicular to the scattering vector is obtained. However, the 3D momentum density can be reconstructed from the measured Compton profiles [53,54,57] or it can be acquired directly with the (γ,eγ) technique [58].

2.5.1 Electron Compton Scattering

Electron momentum spectroscopy [59,60], i.e. electron Compton scattering, is an inelastic spectroscopy technique inherently suitable for ions, molecules, and especially gaseous systems. Compared to the IXS spectroscopy, it basically offers the same information but kinematically in a totally different region. The typical incident energies are well below 1 keV, yet for valence electrons the impulse approximation is still perfectly valid [61]. When combined with the coincidence technique, selective spectroscopy on specific electron shells can be done. The electron Compton scattering technique is more sensitive to the local electronic structure than the Compton technique: the stronger signatures in the scattering spectrum are due to the stronger electron-electron interaction compared to the photon-electron interaction. Further,

the multiple scattering effects play a significant role in the interactions. The electron scattering technique requires vacuum conditions, so it is not as easy to employ as the Compton scattering technique.

2.5.2 Magnetic Inelastic X-Ray Scattering

The interaction (2.6) between an X-ray photon and the spin of an electron is weak but certainly not extinct — it does exist even for completely unpolarized light. Yet, the net effect is directly proportional to the polarization degree, i.e. the extent of the circular polarization, of the incident radiation [62]. In practice, relativistic energies are desired for experimental work. Still, the magnetic contribution to the total scattering cross-section is typically less than 10 %.

The feasibility of the spin-selective IXS spectroscopy was demonstrated fairly early with the circularly polarized γ-ray source ^{57}Co [63]. After the first experiments with synchrotron radiation [64] the technique evolved very quickly [3,47,65–70]. The first dedicated [71] and applied [72] facilities were completed. The theoretical development concentrated on the role of the orbital component in the magnetic IXS cross-section [73]. Experimentally, it was found extinct [74] and finally the absence was explained adequately [75].

Compared to neutrons, magnetic IXS scattering offers essentially the same information on the electronic spin system but only the ferromagnetic materials are easily accessible with X-rays due to the quite small cross-section for magnetic scattering. The low-energy neutrons are significantly more sensitive to the local magnetic structure yielding a appreciably higher signal. The X-ray studies on the spontaneously antiferromagnetic materials are rather difficult because the net effect of magnetization over the sample is zero. Nevertheless, the studies on antiferromagnetic materials under external magnetization have been conducted with IXS but the interpretation of the data is rather complicated [74]. The magnetic experiments using neutrons, however, are typically done utilizing diffraction.

3 Synchrotron Radiation

Synchrotron radiation, first observed in the mid 1940's [76], was long considered an unwanted radiation and energy loss in high-energy electron accelerators. Yet, its well-defined properties were already utilized in the late 1950's for detector calibration [77]. Since the early days, the application of synchrotron radiation has quickly evolved into a standard method for advanced high-accuracy, high-resolution experiments in physical and chemical sciences, even including medicine, life sciences and biology during the 1990's.

In the meantime, the synchrotron radiation sources have gone through three generations. The first-generation sources, circular high-energy electron accelerators, were too faint for any serious scattering experiments, but they were utilized e.g. for detector calibration. The subsequent, more powerful sources, were feasible for some scattering experiments. However, the exploitation of synchrotron radiation was still considered parasitic for the main objective of these machines. In the quest for higher energies by the particle physicists, many of these old parasitic sources were abandoned and later converted to dedicated synchrotron sources. The utilization for spectroscopic studies did not really begin until the 1970's when the second-generation sources, high-energy storage rings (and accelerators) designed and built for bending magnets as the principal emitters of synchrotron radiation, became available. The third generation, fully dedicated storage rings, were designed and built for optimized source properties for synchrotron radiation emitted by the so-called insertion devices. The application of synchrotron radiation has revolutionized the entire field of X-ray physics. For the first time, the source was not the limiting factor for the scientific development. In some cases, the old scientific problems have given rise to new experimental techniques and instrumentation [4].

3.1 Properties

Synchrotron radiation at X-ray energies is emitted by accelerated electrons at extreme relativistic speeds [78,79]. The acceleration is generated either by bending the path of the electron with dipole magnets, or by creating squiggles to the electron's path via periodic magnetic structures, i.e. so-called insertion devices. The internal electromagnetic structure of the modern storage rings is based on a well-defined lattice of straight and curved sections, with dedicated components for controlling the position, divergence and dispersion of the electron beam. In the curved sections, the electron beam is deflected to the direction of the next straight section with bending magnets which are simultaneously used for producing synchrotron radiation. At both ends of the straight sections, the electron beam is corrected with multipole magnets for the position and divergence. The rest of the straight sections is dedicated for the insertion devices. The properties of the electron beam (emittance, divergence) in the

straight sections can be tailored for the type of insertion device chosen. Additionally, a couple of straight sections are typically reserved for the injection line, and for radio frequency cavities to compensate for the dispersion in electron energy, e.g. due to the radiative energy loss of the stored electrons because of the generation of synchrotron radiation.

Bending magnets are the simplest magnetic devices for generating synchrotron radiation. They are still used in modern synchrotrons as they offer easy means for generating continuous X-ray spectrum over wide energy ranges. Yet, due to the deflecting character, the horizontal opening angle of a bending magnet is of the same order as the deflection angle. The insertion devices are periodic magnetic structures placed into the straight sections which force the electrons (or positrons) to swing or wiggle near its trajectory like a sweeping searchlight. In wigglers, the trajectory swings frequently outside the radiation opening cone so the spectra emitted in the different bends of the electron trajectory add incoherently. The intensity of the wiggler radiation thus scales with the number of the magnetic periods. Further, the wiggler spectrum is akin to that of a bending magnet. In undulators, the electron trajectory stays within the opening cone so the radiation emitted within different periods interferes coherently, producing a discrete line spectrum. Due to the interference effects, the intensity of an ideal undulator scales with the square of the magnetic periods. However, the practical outcome depends on the quality of the realization. Furthermore, the third type of insertion device is the wavelength shifter, which basically is a wiggler with one sharp and strong squiggle.

The synchrotron sources are time-structured radiation sources due to the fact that the electrons (or positrons) do not circulate the storage ring as a continuous stream but in discrete bunches, i.e. in short packets, which are separated by a significantly longer time interval than the length of the bunch. The older, pre-third generation sources usually have only a few bunches in the ring, the rest of the ring is empty. Typically, both the inter-bunch time and the orbital period are of the order of 0.1 – 1 μs. With the presently obtainable timing resolution of 10 – 30 ns for the energy-dispersive detectors widely used in the X-ray regime, the source intensity is not at all continuous. However, the third generation sources, e.g. the European Synchrotron Radiation Facility (ESRF) in France, are inherently quasi-continuous sources in this respect. The bunch length in ESRF is of the order of 0.1 ns, the inter-bunch time is 2.8 ns and the orbital period of the storage ring 2.8 μs. Further, the ring circumference is evenly divided into roughly 1000 bunches, 1/3 or 2/3 of which are normally filled like a continuous train of individual bunches. Thus, for the coincidence acquisition system the ESRF storage ring is a quasi-continuous radiation source for 1/3 or 2/3 of the time, the rest of the time the source is essentially equal to a source turned off. The consequences of the quasi-continuity to the coincidence experiments are important (Section 5.1). Furthermore, the internal time structure

of the X-ray intensity can also be exploited by extracting a single pulse of X-rays to the target, e.g. in crystallography of delicate biological specimens like viruses, or in time-resolved studies of the dynamic properties of the target.

Electron energies of the order of $\gtrsim 1$ GeV are required to reach the X-ray range. At this high energies, excellent natural collimation for the photon beam with emitted X-ray intensities several magnitudes above the conventional radiation sources are obtained. The total emitted power easily reaches the kW-range, severely stressing the primary optical components. Furthermore, synchrotron radiation is linearly polarized in the storage ring plane. Above or below the plane, the polarization is elliptical but the handedness is different. However, the obtained intensity drops dramatically off the ring plane. Typically, for 50 % circularly polarized radiation only 10 % of the intensity is left.

The extraordinary properties of synchrotron radiation, i.e. excellent collimation, high intensity, polarization, energy tunability and time structure, offer very exciting possibilities for experiments utilizing high-resolution equipment. The benefits of applying synchrotron radiation for IXS spectroscopy were realized [80] and demonstrated [81] in the late 1970's. The utilization of synchrotron radiation combined to crystal spectrometers for analyzing the scattered IXS spectrum offered a clear advantage over the conventional methods. Equally good or better experimental statistics than before was reached in spite of the improved energy and momentum resolutions. The first magnetic IXS experiments (Section 2.5.2) with circularly polarized synchrotron radiation were proposed already in the beginning of 1980's [64], soon after the ground-breaking γ-ray experiment [63]. After the first synchrotron experiments, magnetic IXS spectroscopy gained momentum steadily during the 1980's. The real revolution started during the 1990's when the dedicated facilities designed for magnetic studies became available.

3.2 The Requirements for Inelastic X-Ray Scattering

IXS spectroscopy spans a quite wide range of both scientific and experimental aims, each with differing combinations of energy and momentum transfers. Yet, the typical requirements for the various types of experiments are quite similar by nature. The physical phenomena relevant for the given regime (Section 2.2) define the desired resolution requirements for the energy and momentum, and for the statistics of the experiment [82]. Contrary to neutron scattering, the energy and momentum transfers in an IXS process are only weakly coupled, offering the benefit of covering ranges in the $\Delta\hbar\omega$-q space inaccessible to neutrons.

The Compton Scattering Regime

To fulfill the requirement for large energy transfer compared to the binding energies, an incident energy of the order of tens of keV is required for targets consisting of medium-Z elements. Scattering angles near the backscattering will ensure that the energy transfer is typically some 10 keV or more for hard X-rays. The large momentum transfer needed is obtained simultaneously. An additional benefit in using the higher energies comes from the absorption cross-sections. For low to medium-Z elements, the IXS cross-section is typically the dominant one. For an ample 0.05 a.u. momentum resolution, the corresponding energy resolution $\Delta\hbar\omega_2/\hbar\omega_2$ should be at least in the range of 10^{-4} but dispersion compensation might be needed [82,83]. However, the energy resolution seems to have an inherent limit in the IXS process due to the interaction of the escaping electron with the rest of the atomic system [36]. The effect is of the order of a few hundredths of a.u. for the lower X-ray energies. At the higher energies, the effect becomes negligible.

The Characteristic Excitation Regime

The incident energy is defined by the sample composition, typically 0.1 – 10 keV is needed depending on the atom and electron shell in question. In terms of the scattered energy $\hbar\omega_2$, the interesting range lies typically 1 eV – 1 keV from the elastic line, with a desired energy resolution better than 1 eV due to the fine resonance structures. A momentum resolution of a few percent of the momentum transfer is usually adequate, as a correct value of energy transfer is typically more important for the physics of the process. The combined requirements require proper selection of the scattering geometry.

The Collective Scattering Regime

The observation of the physical phenomena in this regime requires an extreme energy resolving power of the order of 1 – 10 meV on the scale of 1 meV – 10 eV from the elastic line which obliges using the higher order Bragg-reflections of the analyzer crystal. A momentum resolution of a few percent of the inverse of the characteristic distances is typically enough to study the collective behavior of the electronic system.

3.3 Crystal Spectrometers

The spectrometers utilizing an analyzer crystal to inspect the scattered radiation can be divided into two main types according to the method applied to acquire the IXS spectrum: The scanning crystal and the energy-dispersive spectrometers. All the crystal spectrometers operate in a well-defined geometry where the source (sample), the analyzing crystal and the detector are placed at certain points of the circumference of a common focusing circle, i.e. the so-called Rowland-circle. The practical realization of the analyzer geometry can be done in several different ways,

including either symmetric or asymmetric focusing, and even a slight intentional misalignment of the focusing condition in order to compensate for the source size effects. The various schemes further divide the analyzer crystal geometries into a number of subclasses, e.g. Johann-, Johansson- and Cauchois-types.

The scanning crystal spectrometers record the IXS spectrum sequentially, i.e. one energy (momentum) point at a time, then moving to the next one. The intensity of the scattered radiation is recorded with a detector with no spatial resolution. The incident intensity needs monitoring so that the correct shape of the IXS profile can be recovered. The resolution characteristics of a scanning-type spectrometer are determined typically by the analyzing crystal. Both the intrinsic and geometric properties of the selected reflection, including the bending effects, account to the final resolution figures. 0.1 a.u. is readily reachable, but at 0.05 a.u. and below, dispersion compensation is required [82,83]. At the lower X-ray energies, a record momentum resolution of better than 0.01 a.u. has been reached (Section 3.4.2).

The energy-dispersive spectrometers record the whole IXS spectrum simultaneously, so no incident intensity monitoring is necessarily required. They are realized utilizing position sensitive 1D or 2D detectors, e.g. proportional counters or image plates. Their quite attractive advantages are offset by several other factors like a relatively high background, a need for both accurate energy and efficiency calibration for the whole analyzer-detector combination, and the limited linearity and uniformity of the position sensitive detectors [84].

The modern dedicated IXS facilities utilizing crystal spectrometers have made it feasible to obtain momentum resolutions of the order of 0.1 a.u. routinely with both types. Yet, below 0.05 a.u. the dispersive types are scarce due to the limited spatial resolution for the position sensitive detectors. It can not be compensated arbitrarily by increasing the angular spread of the scattered energy scale by the analyzer crystal, as the increased bending has an adverse effect both on the energy and on the angular resolution of the analyzer crystal. In all cases, a change in the bending properties forces a full redesign of the whole analyzer geometry.

The relative merits of the different types are strongly dependent on the practical realization. Given the targeted figure of momentum resolution within a given incident energy range, there are no correct spectrometer types nor correct designs. The only restriction comes from crystal X-ray optics itself. Higher order reflections are required for a higher energy resolution. On a regular basis, when designing a new IXS beamline the decision on the type of the spectrometer is based on earlier experience, together with possible trials on the new designs. The whole IXS beamline has to be designed as one entity. Other merits, like the experimental accuracy obtained during one day or the overall stability during long experiments, are largely determined by the properties of the synchrotron source and the quality of the incident intensity monitoring (Section 4.1).

3.4 Facilities for Inelastic X-Ray Scattering Spectroscopy

The rich variety of physical phenomena encountered with IXS spectroscopy prevents construction of a single type of an IXS facility suitable for everything. The features accessible depend on the experimental conditions. Additionally, the signatures relevant for the given type of IXS process are found in different parts of the acquired spectrum, resulting in differing requirements for the characteristics of the spectrometers (Section 3.2). Several dedicated IXS facilities exist, each with different prospects. Five of those are introduced, with some remarks on the focus of the instruments. They differ quite distinctively by design. The ID15B (Section 3.4.1) built at the European Synchrotron Radiation Facility (ESRF) in France is a sophisticated focusing scanning crystal design with fixed incident energies. The X21A3 (Section 3.4.2) at the National Synchrotron Light Source (NSLS) in the USA is a modern high-resolution design which offers more flexibility, allowing both the incident and scattered energies to be scanned independently. The Japanese realizations (Section 3.4.3) employ a totally alternative design approach utilizing energy-dispersive optics and an image plate for analyzing the scattered radiation. Finally, some other designs are briefly discussed.

3.4.1 ID15B (ESRF)

The ESRF storage ring is a third generation synchrotron radiation facility with a 6 GeV electron energy. The radiation source for the high-energy IXS beamline ID15B is either an asymmetrical multipole permanent-magnet wiggler or a superconducting wavelength shifter, for which the critical energies are 45 keV and 96 keV, and the vertical opening angles of the radiation cone are $\pm$ 2.2 mrad and $\pm$ 6 mrad, respectively. The wiggler source provides circularly polarized radiation above and below the orbit plane of the storage ring for studies of magnetic materials. Cylindrically bent, asymmetrically cut Johann-type, horizontally focusing Si (111), (220) or (311) monochromators with a demagnification ratio of 5:1 serve the beamline with an energy band $\Delta E/E$ of $\sim 3 \cdot 10^{-4}$ at incident energies of 30, 50, and 60 keV, respectively. The monochromator construction allows for a tunability of 15 % in the incident energy. The incident monochromatic photon flux is in the range of 10^{11} – 10^{12} s^{-1}, obtained with typical entrance collimating slits of 0.2 mm (H) $\times$ 5 mm (V).

The spectrometer [85] is based on an advanced scheme following the Johann-geometry, i.e. the analyzer crystal is bent cylindrically to a radius equal to the diameter of the focusing circle. Already the preliminary studies conducted on a prototype spectrometer proved the concept realizable [86,87]. The IXS spectrum is recorded sequentially by rotating the Si (400) or Ge (440) analyzer crystal and maintaining the focusing geometry with synchronized rotations and translations of the analyzer and the detector (a NaI scintillation detector). The sample stage can

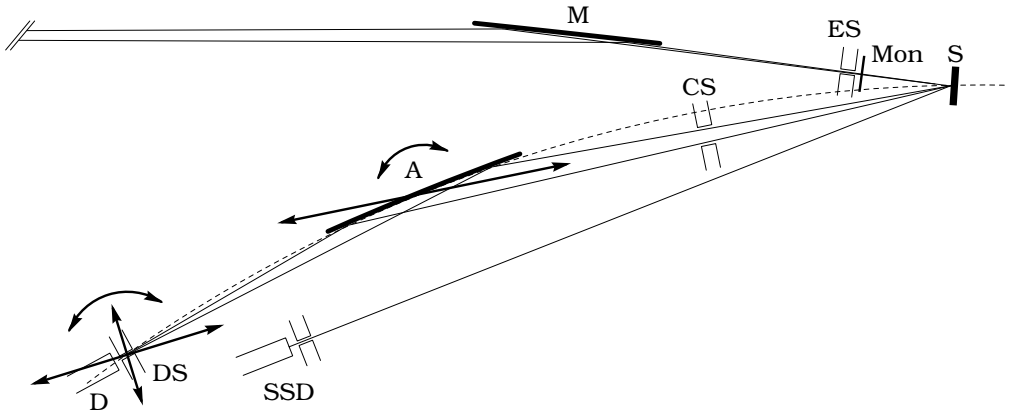

Fig. 1. Schematic layout of the ID15B (ESRF) IXS spectrometer (not in scale). The incident radiation is monochromatized and focused (**M**), and collimated (entrance slits **ES**) to the target (sample **S**). The analyzer (bent crystal **A**), collimator (detector slits **DS**), and detector (NaI scintillation detector **D**) acquiring the scattered spectrum are on the Rowland-circle (dashed line). The radius of the Rowland-circle remains constant during the scan, but the analyzer and detector positions do change. Both the incident beam and the scattered spectrum are monitored, with a Si PIN-diode (**Mon**) and a Ge solid-state detector (**SSD**), respectively.

carry cryostats, magnets or even high-pressure equipment. Further, it can be translated longitudinally or transversely, lifted, rotated and tilted on all three axes. The incident intensity is monitored by two separate means, i.e. with a Si PIN-diode for the incident beam right after the entrance slits, and with a solid-state detector for the radiation scattered by the target. The secondary monitor is further enhanced by extracting only the spectrum of the IXS profile and the elastic line. Additionally, the countrates in the monitors are fed to the `spec`™ acquisition and control system [88]. In the case of a beam loss, the data acquisition is suspended, and later on beam recovery is continued automatically. The primary monitor for the incident beam is used to normalize the acquired data.

The analyzer crystal might produce some parasitic contributions to the detected spectrum due to the off-plane reflections. These contributions can be avoided or minimized by proper selection of the analyzer crystal cut, incident energy and scattering angle. Additionally, a scheme based on fitting the various background components in the spectrometer detector spectrum gives an opportunity to remove the parasitic components. The background not originating from the sample is typically well below the 1 % level of the maximum of the Compton profile. Typically, countrates of 1 – 10 kcps at the Compton peak are obtained, thus allowing the acquisition of the profile with 0.1 % statistical accuracy at the profile peak in one day.

The spectrometer is optimized for IXS experiments with a decent momentum

resolution of 0.15 a.u. at the incident energy of 60 keV (0.08 a.u. at 30 keV) but with a high statistical accuracy in the Compton regime. In the future, the design will be updated, e.g. to apply dispersion compensation [82,83] to reach a momentum resolution of 0.05 a.u. at the incident energy of 60 keV. Additionally, the excellent stability of the ESRF storage ring together with the high-precision monitoring makes high-accuracy scanning-type spectrometers feasible providing low background and selective recording of the interesting parts of the full IXS spectrum. Further, even specimen consisting of appreciable amounts of medium-Z elements, which are in many cases important components in many interesting novel materials, can be studied because of the low absorption of the high-energy X-rays.

3.4.2 X21A3 (NSLS)

The beamline X21A3 is optimized for incident energies of the order of 8 keV for several different types of IXS experiments: Compton scattering, valence-band excitations, resonant and non-resonant Raman scattering [89,90]. The low incident energy limits the targets to low-Z materials (inner-shell, or atomic features), or to samples consisting of low-Z to medium-Z elements (valence electron features). The widths of the relevant features in the IXS spectrum range from meV to several hundreds of eV. The valence excitations and the non-resonant Raman process require the measurement of the energy loss as a function of the incident energy. The resonant Raman process makes changes of both the incident and scattered energies necessary. The energy resolution of the spectrometer is essentially constant within the energy range of interest. For Raman scattering, no superior momentum resolution is needed, so the resolution has been compromized for higher scattered intensities. For valence-band excitations, good momentum resolution is more important. Thus, the construction allows for enhancing the resolution to a more decent level with limiting the angular size of the analyzer crystal.

The NSLS storage ring is of a second generation design. The electron energy of 2.5 GeV makes the ring best suitable for producing X-rays in the range of 0.1 – 10 keV. The radiation source for beamline X21A3 is a hybrid 27-pole wiggler with a critical energy of 4.6 keV and characteristic opening angles of $\pm$ 1.25 mrad (H) and $\pm$ 0.125 mrad (V), respectively. The X21A3 optics consists of two Si double-crystal monochromators in a dispersive anti-parallel setup, and a focusing mirror. Both crystals are channel-cut, with one symmetric and one asymmetric (220) reflection with a miscut of 16°. The incident energy resolution, incident intensity and the focal point remain essentially unchanged over the entire scannable incident energy range of 6 – 10 keV. The incident monochromatic photon flux of $\sim 5 \cdot 10^{10}$ s^{-1} at the target is obtained with an energy resolution of 220 meV to a focal point size of 0.3 (H) $\times$ 0.5 (V) mm^2 and a negligible angular divergence of 11.6 arcsec. The scattered fluxes range from 0.1 cps to 10 kcps, strongly depending on the type of

scattering process and target.

The spectrometer is based on a spherically bent ($R = 1$ m) Johann-type symmetric focusing Si(444) analyzer crystal ($\varnothing = 90$ mm), operating close to the backscattering geometry. The diffracted backscattering energy of the (444) reflection, 7908.5 eV, matches perfectly with the source properties. The intrinsic width of the (444) reflection is ~ 40 meV. Yet, the simulated final resolution of the analyzer crystal increases to 190 meV mainly due to bending but also due to source size effects. The final experimental energy resolution for the scattered radiation at the elastic line is 280 meV. The momentum resolution varies between 0.28 a.u. (at $q = 0.15$ a.u.) to 0.06 a.u. (at $q = 4.14$ a.u.) when the entire analyzer crystal is in use. By slitting down the size momentum resolution can be enhanced to 0.01 a.u. roughly.

The sophisticated design makes advanced experiments at scattering angles ranging from a few degrees up to 170° feasible, covering a very wide selection of energy (0 – 1 keV) and momentum transfers (0 – 10 a.u.). Independent studies on the energy and momentum transfer dependencies of the IXS process the other entity fixed are possible. Precision control of the instrument, together with high-accuracy performance and efficiency analysis of the spectrometer, opens up new interesting chances to experimental work in this particular field of IXS spectroscopy. The reference [89] provides several excellent examples of the capabilities of the spectrometer.

3.4.3 BL14C (Photon Factory), NE1 (KEK), and BL08W (SPring-8)

These beamlines share the same basic design despite of the fact that they are constructed for different storage rings. The common denominators are a wiggler as an X-ray source, a single one-bounce bent-crystal monochromator and a Cauchois-type Si(422) crystal bent to a curvature of ~ 2 m, together with a position sensitive detector for the analysis of the scattered radiation. The BL14C [91], located at the 2.5 GeV storage ring of the Photon Factory, is optimized for an incident energy of 29.5 keV. The other two, installed at the high energy storage rings of KEK [92] and SPring-8 [93], (6.5 and 8 GeV electron energies, respectively) are optimized for higher incident X-ray energies of 40 – 70 keV and 100 – 300 keV, respectively. The NE1 utilizes four sets of identical analyzer crystals arranged on the surface of a cone and sharing the same scattering angle, allowing the acquisition of the scattering spectrum along four different crystal directions simultaneously. Additionally, the BL08W is capable of magnetic studies at a somewhat worse momentum resolution of 0.5 a.u..

For the incident energy, these beamlines present a common relative bandwidth of $\sim 10^{-3}$. The resolution in the scattered energy is typically a factor of 2 better, yet limited mainly due to the source size effects. However, the momentum resolution — 0.10 a.u. (BL14C), 0.13 a.u. (NE1) and 0.08 a.u. (BL08W) — is in every case limited by the spatial accuracy of the detector (a gas proportional counter for BL14C, an image plate for the others). Additionally, the image plates pose an inherent

0.5 % precision limit for the experiment due to the inhomogeneity of the detection efficiency [84]. The integrated countrates are typically of the order of 10 – 50 cps (BL14C and NE1) to 400 cps (BL08W) with a signal-to-noise ratio of 20 – 30.

The advantages of the design chosen are obvious. The spectrometers are quite simple in construction, stationary and easy to control and operate. No monitoring for the incident intensity for the normalization of the acquired data is required. The whole scattering spectrum is recorded simultaneously. For high-accuracy work, the drawbacks are severe. The 0.5 % precision of the image plates limits the applicability of the beamlines to high-accuracy experiments (Section 6.2). Further, the precision of the efficiency calibration for the analyzing system is limited due to the same reason. The systematic error does not cancel out, as the inhomogeneity depends on the actual plate used.

3.4.4 Other Designs

The first operational IXS facility utilizing synchrotron radiation was the one installed at LURE, France [81]. Since then, it has been updated but keeping the basic design intact. ESRF has an another IXS beamline dedicated for ultra-high resolution spectroscopy [94] with an scattered energy resolution of the order of 1 meV. Applications in this resolution range include e.g. studies of collective excitations, like the fast sound in water [95]. The German synchrotron DORIS-II had a dedicated IXS beamline INELAX [96] which was designed with phonon scattering studies in mind, while the spectrometer at the newer HARWI-Compton beamline (DORIS-III) is a redefined design for the new radiation source but with dispersion compensation [83]. The HRIXS beamline at the Advanced Photon Source, USA, is very similar to the X21A3 in design [97]. A four-bounce monochromator provides 5.2 meV energy resolution at incident energies of the order of 14 keV, and the bent analyzer crystal yields total energy and momentum resolutions of 7.5 meV and $\lesssim 0.05$ a.u., respectively.

4 Experimental Accuracy

The acquired IXS spectrum contains two kinds of intrinsic inaccuracies: both the error $\Delta J(p_z)$ due to the counting statistics and the finite momentum resolution Δp_z of the spectrometer, limit the applicable accuracy of the experiment. Additionally, a number of extrinsic error sources do exist. They arise from the setup of the experiment, from the experimental equipment, or are due to other physical processes occurring simultaneously in the system. In typical experiments with conventional radiation sources, most of them are of minor significance due to the higher experimental errors, or they are assessed to adequate precision by using quite simple physical models due to the not-so-strict accuracy requirements. However, the state-of-the-art crystal spectrometers designed to match and fully utilize the extraordinary source properties of the third generation synchrotron radiation sources allow the acquisition of the IXS spectra down to 0.1 % statistical accuracy at the profile peak in one day. In order to truly attain this high accuracy level, the conditions for data consistency and reliability should be carefully examined. Insight in the factors affecting the quality of the data is needed so that the experimental accuracy available can be exploited without unnecessary restrictions. The factors considered here include several issues which are especially important for the experiments conducted on synchrotron sources, e.g. the normalization and consistency of the acquired data, but also some other questions that affect the quality of the experiment regardless of the type of the radiation source.

4.1 Data Normalization

The incident intensity striking the target at a synchrotron source requires continuous monitoring as it is a time-dependent but non-deterministic phenomenon. Yet, the quantity determined in the experiment, the scattering cross-section, is time-independent provided no changes occur in the sample. Thus, the acquired spectrum must be normalized with the incident intensity to extract the true drift-free spectrum and its error, i.e. the experimental statistics.

Typical monitoring techniques include gas ionization chambers, Si PIN-diodes and solid-state detectors, which each have their pertinent merits. Gas ionization chambers are one of the simplest X-ray detectors known, offering excellent linearity and comprehensive dynamic range up to the level of the incident intensities at synchrotron sources yet no energy nor event resolution. Similarly to the gas ionization chambers, Si PIN-diodes are typically utilized coupled to a low-noise charge-sensitive preamplifier, giving the output as a current dependent on the intensity with good linearity and wide dynamic range. Solid-state detectors offer adequate energy resolution for inspecting the spectrum of the radiation monitored. However, the dynamic range is severely diminished which can be overcome by looking at the radiation scattered

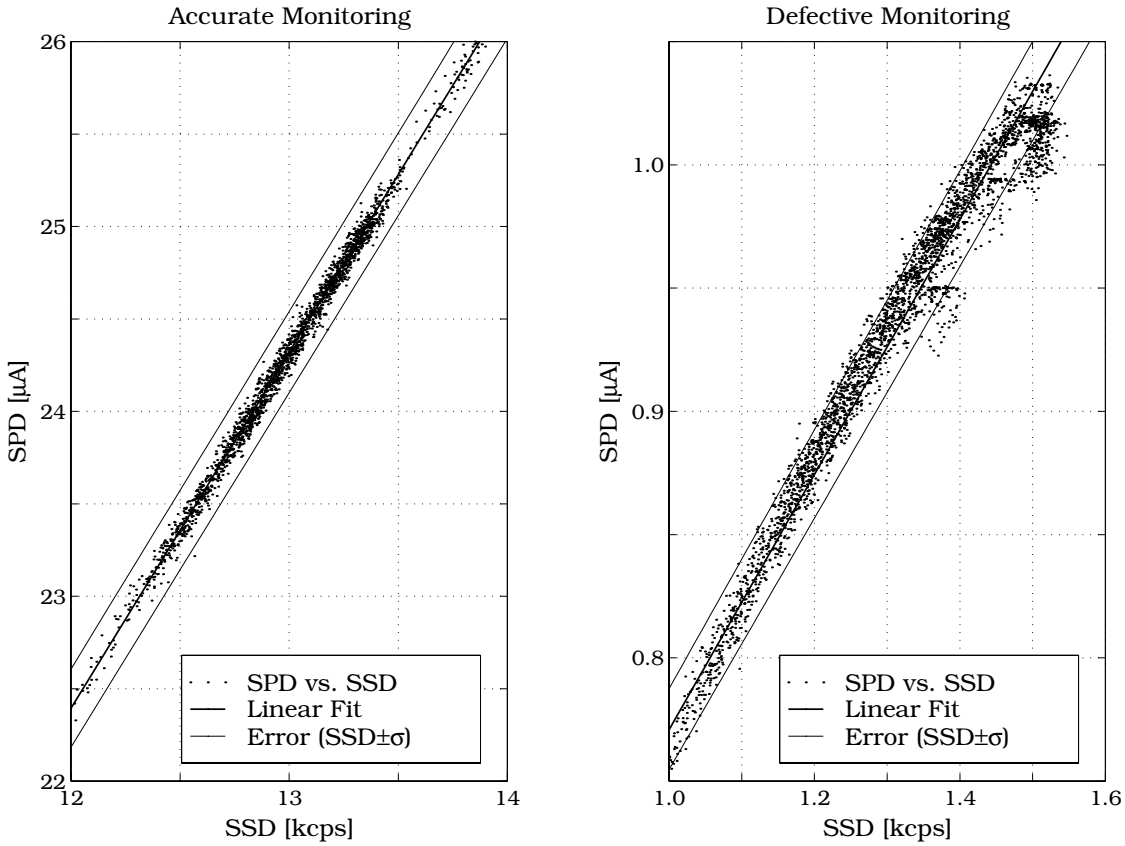

Fig. 2. Examples of accurate and defective incident intensity monitoring at the ID15B (Section 3.4.1). The anomaly discovered in the defective case was due to the inadequate sampling rate of the picoammeter used for the Si PIN-diode.

by the target. Si PIN-diodes can also be used as energy-dispersive detectors, but with a likewise significantly lowered dynamic range. In typical applications, solid-state detectors and the energy-dispersive Si PIN-diodes are accuracy-limited devices due to the counting statistics but gas ionization chambers and the current-mode Si PIN-diodes are precision-limited.

The employment of two individual intensity monitors of different types, or in different working schemes, provides an additional method of checking the consistency and performance of the monitoring. Apart from an efficiency scaling factor, both monitors should give out identical information. Additionally, utilization of a solid-state detector (or an energy-dispersive Si PIN-diode) as one type provides an accuracy-limited reference against which the severity of the deviations possibly found can be evaluated. However, the responses of the monitors to the harmonics of the source are different. In most cases where the anomalies are small, the adverse effects are not directly seen in the data but they can still ruin the result of the experiment. By comparing the two monitors, e.g. Fig. 2, the anomalies are easily exposed.

4.2 Data Consistency

The practical realization of the scanning crystal spectrometers forces the acquisition of the full IXS spectrum sequentially, i.e. again and again in successive runs, adding a further potential error source to the experiment. After the normalization with the incident intensity, the repeatedly acquired individual spectra (recorded for the given target orientation, for example) are expected to be equal. The equivalence should not be restricted only to the individual spectra being equal within the statistics. It must include the requirement that the relevant details in the acquired spectra, e.g. the intensities, positions, shapes and asymmetries of the given peaks, remain unchanged during the experiment within the expected error limits. The discrepancies in these quantities are quite typically independent of the experiment statistics. Yet they do surely depend on the practical conditions chosen to realize the experiment.

In IXS experiments, the most important peak properties to keep in mind are those of the IXS profile itself. The significance of the variations in the characteristics of the elastic line depend on its deviations relative to those of the IXS profile: a drift common to both is much easier to correct than one having a different effect on each. The peak characteristics of the elastic line reflect mostly the stability of the incident beam in energy, position and intensity, which in turn are entirely dependent on the performance of the monochromator under the varying heat load conditions. The fluorescence lines in the spectrum can also be used, e.g. for checking the stability of the rest of the experimental apparatus since their position is independent on the incident energy.

The unequal physical shape of the sample in the given crystal directions introduces slight changes into the scattering angle when the position of the target is optimized for the spectrometer. The effect should be restricted well below the angular resolution of the spectrometer, or the sample shape must be altered. In terms of the physics of IXS, the scattering angle effects might be of minor importance but the utilizability of the full data set acquired in different crystal directions relies on similarity. This is especially important when the directional differences are taken.

The directional differences, i.e. the anisotropies between the two given IXS profiles, set a further requirement for the quality of the data. The measurement geometries should be as equivalent as possible so that the correction factors applied to the data are sufficiently akin. However, this does not necessarily demand the use of a sample (or samples) identical by shape relative to the respective crystal directions. The same specimen can even be measured in different scattering geometries, e.g. in the transmission and reflection geometries, but all the corrections applied, e.g. the absorption correction, should be known accurately enough so that no extra errors are added due to the difference in geometry. Nevertheless, in most cases the use of separate samples for each direction requires significantly less effort.

4.3 Background Corrections

All components in the acquired spectrum not directly related to the IXS process itself, or considered as secondary processes occurring after the primary IXS process, constitute the background. It can develop either in the sample, e.g. due to other processes like photoabsorption, or in the external environment, e.g. spurious scattering from the experimental equipment. The latter can be defeated by appropriate collimation and shielding (Section 4.6). Nevertheless, the former must be subtracted in order to extract the true IXS profile, free from any artificial contributions. In properly designed IXS experiments, the characteristic fluorescence lines do not overlap the IXS profile. Thus, the spectral background components remaining in the range of the profile are mostly due to *Bremsstrahlung* (Section 4.3.1) and multiple scattering (Section 4.3.2).

4.3.1 Bremsstrahlung

The IXS experiments carried out at the modern synchrotron sources typically utilize the hard X-ray region of 10 – 100 keV. For targets consisting predominantly of low-Z to medium-Z elements, the principal scattering process is the IXS. For higher-Z materials, photoabsorption becomes dominant. Either way, both processes create free electrons in the sample. While decelerating, the electrons emit Bremsstrahlung [98–100]. The Bremsstrahlung spectrum is similar for both cases, but certainly not identical, due to a delicate difference in the scattering processes creating the free electrons. For monochromatic incident photons, the kinetic energy of the photoelectrons, i.e. the free electrons created via the photoabsorption process, is precise, and the electron escape cone is well-defined. For non-polarized incident radiation, it follows the familiar $\hbar\omega_2^{-1}$ energy dependence [30]. Yet, the same is not entirely true for the Compton electrons which are created by the IXS process. Their kinetic energies are inherently distributed, closely related to the IXS profile. The escape cone is thus more diffuse and the full Bremsstrahlung spectrum has to be integrated because the tabulated spectra are typically given for monoenergetic electrons only. Also the spectral shape is altered slightly. Additional weight is shifted towards lower energies if compared to the spectrum emitted by photoelectrons of identical (maximum) kinetic energy. For a given incident photon energy, however, the Bremsstrahlung spectrum due to the Compton electrons is typically found at significantly lower energies than that due to the photoelectrons, and it seldom overlaps the energy region of the IXS valence profile. The photoelectron Bremsstrahlung contribution is still prominent in the range of the core profile and in most cases also overlaps the IXS inner-shell spectrum. An adjustment of the scattering geometry to minimize this component is beneficial.

The Bremsstrahlung background problem was encountered fairly quickly when IXS experiments of high enough statistical accuracy in the relevant energy region were established [101–106], in particular the coincidence experiments were affected [30,31,107,108,128], [**Paper II**]. Although the effects due to the much anticipated failure of the impulse approximation in IXS experiments are modest, some of the key questions, e.g. the infrared divergence [28] (Section 2.4), will remain unresolved experimentally until a reliable way to subtract the Bremsstrahlung component is established [**Paper II**]. However, the physical modeling of Bremsstrahlung has taken notable advances during the recent years [109].

4.3.2 Multiple Scattering

The probability of having several scattering events per single incident X-ray photon is directly dependent on the effective thickness of the target. If the effective thickness is significantly higher than the real dimensions of the sample, the fraction of photons scattering more than once before leaving the sample is negligible. However, for the incident energy range of 10 – 100 keV the effective thickness typically approaches the real dimensions of the target making the multiple scattering effects clearly visible. In most cases a compromise between a clean signal with no detectable multiple scattering events, and a countrate high enough but with a significant multiple scattering contribution treated properly has to be made.

The methods to calculate the multiple scattering corrections for the IXS spectra are well-established. It can be done either by extrapolating the experimental results obtained with targets of different thicknesses to zero thickness [110,111] or by means of Monte-Carlo simulations of the various multiple scattering contributions [112–115]. However, the importance of the corrections seems to depend on the scattering regime (Section 2.2). For the characteristic excitation regime the correction is typically of the order of a few percents [114] but in the Compton scattering regime with low-Z targets a significant portion of the acquired IXS spectrum can be due to the multiple scattering [115].

4.4 Momentum Resolution

The finite momentum resolution Δp_z of the spectrometer limits the distinctiveness of the features seen in the IXS spectrum. Any spectral details sharper than or near the resolution limit are smeared. As the momentum scale p_z is dependent on the three experimental parameters, namely $p_z = p_z(\hbar\omega_1,\ \hbar\omega_2,\ \varphi)$, the momentum resolution Δp_z is a function of the errors in the same parameters (4.1)

$$\Delta p_z \;\simeq\; \sqrt{\Big(\frac{\partial p_z}{\partial \hbar\omega_1}\,\Delta\hbar\omega_1\Big)^2 + \Big(\frac{\partial p_z}{\partial \hbar\omega_2}\,\Delta\hbar\omega_2\Big)^2 + \Big(\frac{\partial p_z}{\partial \varphi}\,\Delta\varphi\Big)^2}\,. \tag{4.1}$$

The individual parameters $\hbar\omega_1$, $\hbar\omega_2$, and φ are not entirely independent. A shift in one parameter introduces corresponding changes to the others so that (2.3) holds for the chosen experimental conditions. Additionally, in order to sum up the individual errors in the root-squared style (4.1) as independent variables require, the inaccuracies in the variables are expected to follow the Gaussian distribution, a condition which not always completely true. For instance, on synchrotron sources the line shape of the incident energy is far from a symmetric Gaussian although it is typically narrow enough not to dominate the final momentum resolution. However, in properly designed beamlines (and in properly accomplished experiments) the errors or shifts in the parameters during the experiment are so small that the inter-dependencies and the non-Gaussian behavior can be overlooked and the equation (4.1) can be safely used to determine the momentum resolution. The individual partial differentials in (4.1) can be calculated from (2.3).

The partial differential for the incident energy $\hbar\omega_1$ is typically constant in $\hbar\omega_2$ in the range of the IXS profile. The non-linearity of the partial differential for the scattered energy $\hbar\omega_2$ is usually significantly higher due to the energy dependence of the energy resolution of the detector, be it a solid-state detector or a analyzer crystal together with a scintillation detector. The partial differentials for the incident and scattered energies both contribute of the order of $100{\cdot}\big(\Delta\hbar\omega_{1,2}/\hbar\omega_{1,2}\big)$ a.u. roughly to the momentum resolution. However, the partial differential for the scattering angle φ is strongly dependent both on φ and $\hbar\omega_{1,2}$, reflecting the fact that the energy transfer in the IXS process is asymmetric in φ.

In the modern synchrotron sources, the contribution to the final momentum resolution from the incident energy term is typically minor due to the usual designed energy resolving powers of $\sim 10^{-4}$ for the primary optical systems. The contribution from the scattered energy resolution is usually higher, in many cases it is the dominant one. The X21A3 (Section 3.4.2) is an important exception. It utilizes the lower incident energy range of the order of 10 keV and the backscattering analyzer geometry for an extreme energy resolving power of $\sim 10^{-4}$ in $\hbar\omega_2$. There, the geometric partial differential contributes the most to the momentum resolution. The scanning crystal spectrometers utilizing the higher X-ray energies, e.g. the one at the beamline ID15B (Section 3.4.1), normally achieve an energy resolving power of $\sim 10^{-3}$ in $\hbar\omega_2$, yielding a final momentum resolution of ~ 0.1 a.u..

4.5 Geometric Effect

The geometric effect arising from the inaccuracy in the scattering angle, i.e. divergence, does play a discernible role in the high accuracy IXS experiments. The geometric partial differential is highly asymmetric in φ around the 'correct' scattering angle, both as a function of $\hbar\omega_1$ and $\hbar\omega_2$, only reflecting the fact that the energy transfer itself in the IXS process is asymmetric in the scattering angle around the 'correct' φ. The IXS spectrum is recorded as a function of $\hbar\omega_2$, not p_z. Thus the $\hbar\omega_2$-scale is common for the entire detector but the exact position of $p_z = 0$ in $\hbar\omega_2$ varies over the detector aperture due to the divergence $\pm\Delta\varphi$ in the scattering angle. Consequently, due to the fact that the irradiated target and the detector have finite sizes, an inherently asymmetric contribution to the total Δp_z is introduced and the asymmetry of the Compton profile is increased.

Solid-state detectors typically exhibit the biggest geometric effect due to the relatively large aperture compared to the short viewing distances, especially with conventional radiation sources. On synchrotron sources, solid-state detectors are used at larger distances which diminishes the effect. Crystal spectrometers do also suffer from the geometric effect, although it typically is an insignificant factor. However, the scanning crystal spectrometers have another similar but additional property: the change in the angular size of the target during the scan, as seen by the analyzer crystal. In a properly designed spectrometer these geometric effects should not play a discernible role in the total Δp_z, nor in the asymmetry of the IXS profile. The most important question is whether the asymmetry due to geometric effect is significantly higher than due to the finite energy resolution. From a mathematical point of view, the smearing of the details in the IXS spectrum due to the finite momentum resolution conforms to convolution. Convolution with a symmetric, yet variable-width instrument function is essentially equal to convolution with an asymmetric yet constant-width instrument function. Both operations introduce asymmetry to any peak profile.

Within the impulse approximation, the IXS profile $J(p_z)$ is symmetric. However, a residual asymmetry has been observed in several experiments after applying all the relevant correction factors to the acquired IXS spectrum [116–119]. Additional to the Compton defects (Section 2.4), several other explanations have been given, e.g. the line-shape properties of the incident radiation [120], or self-scattering in the radiation source [121]. The role of the geometric effect has been emphasized earlier [118] but no simulations on the effect in the quantitative level were done at that time.

4.6 Shielding and Collimation

The purity of the acquired IXS spectrum is largely dependent on the success in preventing the detector from seeing any spurious scattering events in the IXS spectrum. The term cleanness is, of course, defined by the experiment. In an IXS experiment with no coincidence conditions, the background is normally subtracted with the aid of the theoretical core profiles. For a linear or smooth background this procedure works well but in case of a more complex background component, part of it might end up being a portion in the observed anisotropy. A separate measurement of the background contribution should be done to get a good idea of the situation. With proper collimation, the cleanness of the IXS spectrum can be warranted [**Papers II, IV**].

The danger of acquiring artificial contributions to the IXS spectrum is especially high in coincidence experiments. Only an appreciably small part of the total IXS spectrum is selected for acquisition with the aid of simultaneity and energy conditions. Thus, a relatively weak secondary process may produce a significant contribution to the final spectrum if the conditions are fulfilled [30], which can also lead to erroneous results [33,122]. With a well-designed shielding and collimation procedure, the artificial by-products can be defeated entirely [**Paper II**].

5 Experimental Challenges

The Compton scattering technique is a relatively old tool compared to the other X-ray spectroscopy methods. In terms of carrying out the experiments in practice, the Compton technique has several crucial advantages (Section 2.5), but the physical nature of the IXS process as an incoherent scattering process limits its applicability. The knowledge of the behavior of the interesting valence electron states is dependent on the successfull subtraction of the core contribution from the acquired IXS spectrum. Within the impulse approximation, the calculation of the Compton profiles for the individual electron shells is straightforward. However, the limits for the validity of the impulse approximation are not yet that well-defined (Sections 2.4 and 5.1).

The recent advances in the experimental methods used in IXS research, mainly due to the advent of the synchrotron radiation, have made high-resolution high-accuracy IXS spectroscopy feasible [123]. At the same time, theoretical methods have improved considerably [124]. The electronic properties of the ordinary solid-state materials, e.g. the elements (Section 5.3) or the binary metal alloys (Section 5.2), can nowadays be modeled quite accurately even though the significance of the correlation effects in the IXS process is an issue not yet thoroughly understood [125]. However, the advanced exotic materials, e.g. high-T_C superconductors (Section 6.1) or quasicrystals (Section 6.2), still persist or even deny satisfactory understanding of their electronic properties. In these cases, IXS can provide valuable information on one of the most fundamental electronic properties, the electronic momentum density.

5.1 Coincidence Technique

The prevailing assumption for the validity of the impulse approximation (Section 2.4), that is $\Delta(\hbar\omega) \gg E_B$, can fail for the deeply-bound electrons. With X-rays, this condition is encountered fairly effortlessly for the inner-shell electrons of the medium-Z elements, a situation which has given rise to several experiments in order to reveal the possible effects due to the failure of the impulse approximation in the inner-shell IXS spectrum [3]. The contribution of a given electron shell to the total IXS spectrum can be extracted with the coincidence technique. The inelastically scattered photon is detected in coincidence, i.e. simultaneously, with the characteristic fluorescence photon which is created when the inner-shell hole left by the ejected Compton-electron is filled. For the detectors (and timing electronics) presently available to resolve the simultaneity condition, this happens instantaneously.

The coincidence experiments have been done primarily with various radioactive sources [3]. Both the experiments [30,31,33,126] and the predictions based on various theoretical models [13,27,32–34] preceding the [**Paper II**] have given somewhat inconsistent results: The failure of the impulse approximation has been predicted to be the origin of Raman-like resonant structures seen in the scattering spectrum [33],

contradicting the standard one-electron $\mathbf{A}^2$ description of IXS scattering from quasi-free electrons. On the other hand, impulse approximation has been found to work well even in the intermediate momentum transfer region [13,31,32]. Further, the features observed in [33] were presumably due to false coincidences generated by the ill-defined setup of the detectors [122]. Yet, the primary deficiency in nearly all of the previous experiments is their inadequate statistical accuracy for direct quantitative comparison with theory. In the only successful experiment [31], only the shape of the IXS core-shell profile was recovered, not the absolute cross-section needed for a direct comparison.

With monochromatized and focused X-rays the counting efficiency is improved significantly due to the better-defined scattering geometry [**Paper II**]. Furthermore, the normalization of the IXS cross-section can be done reliably in the absolute scale by determining the incident intensity in the same geometry. Surprisingly enough, the impulse approximation does seem to work quite well in the intermediate momentum transfer region [**Paper II**], which is confirmed by the advanced quantum-mechanical S-matrix calculations [32]. Further, it was shown very recently that the impulse approximation actually should give the doubly-differential IXS cross-section quite accurately even in the intermediate momentum transfer region, but it is not anymore employable for the triply-differential cross-section in the same region [127].

Synchrotron sources were previously thought to be badly suitable for coincidence experiments due to their non-continuous time structure (Section 3.1) which leads to a significant increase in the countrate of the chance coincidences [30,128]. The third generation synchrotron sources, e.g. the European Synchrotron Radiation Facility in France, are inherently more eligible for coincidence experiments as their characteristic time scales are shorter than, or similar to, the best experimental timing resolutions achieved. Thus, the storage ring is effectively a quasi-continuous radiation source for the coincidence acquisition system, rendering the adverse effects due to the discrete time structure to the countrate of the chance coincidence events negligible [**Paper III**]. However, the proper optimization procedure for the experimental parameters to obtain the best counting performance is quite different from that for the conventional sources.

5.2 Topology of the Fermi Surface

According to the free-electron theory, the electronic states in a metallic, i.e. conducting, material are filled up to a given energy, the Fermi energy (E_F). Correspondingly, in the momentum space the electrons occupy a volume, which is bounded by the so-called Fermi sphere. The surface of the sphere is the Fermi surface and the radius of the sphere gives the Fermi momentum p_F. In real metals, the Fermi surface topology is modified by the solid-state effects, e.g. the periodic ion-core potential

(which reflects the crystal structure and symmetry) and impurities (or doping). The effects to the Fermi surface due to the crystal structure are seen mostly in the vicinity of the Brillouin-zone boundaries.

Elucidation of both the spatial extent and occupation of the ground-state electron wave functions is essential for the understanding of the electronic and transport properties of solid-state materials. The topology of the Fermi surface reflects the electronic density of states in terms of the electronic momentum density. Both the momentum density and the Fermi surface dimensions in the important symmetry directions can be extracted from the Compton profiles, as they are the projections of the electronic momentum density along the crystal directions in question. Thus, IXS spectroscopy provides a probe to directly study the structure of the Fermi surface.

The first-period transition-metals form quite interesting alloys with aluminum covering the entire concentration range. Great efforts have been made to study the nature of bonding and charge transfer in these alloys [129]. The bonding is characteristically covalent, including hybridization of the Al s and p orbitals with the transition-metal d orbitals, and net charge transfer from Al to the transition-metal sites. The ordered equiatomic Al alloys, e.g. FeAl, CoAl and NiAl, crystallize in the simple CsCl-structure.

The previous IXS studies on polycrystalline FeAl, CoAl, and NiAl [130] failed to reveal the remarkable anisotropy predicted [131]. Preliminary experiments on single crystals grown by the Bridgmann-method utilizing a W $K\alpha_1$ X-ray spectrometer [132] showed only the gross features. Finally, experiments with the high-resolution spectrometer at the beamline ID15B (Section 3.4.1) recovered the anisotropy [**Paper I**], as predicted with the recently developed scheme based on the full-potential linearized augmented-plane-wave method [133]. Even the Fermi surface signatures originating from a single partly-filled valence shell could be recovered reliably.

5.3 Electron Correlation Effects

The free electron gas has attracted considerable attention for more than half a century, mainly because it provides an excellent testing ground for the numerous theoretical models. The electron-electron interaction, which modifies the shape of the Fermi surface additionally to the solid-state effects (Section 5.2), is one of the most important features in the behavior of the free electron gas. As a result of the interaction, some of the conduction electrons in states $p < p_F$ get excited to states $p > p_F$. The discontinuity in the occupation number at p_F persists, but its magnitude is lowered. The extent of the changes in the occupation number is reflected in the momentum density of the conduction electrons [54].

The free electron gas is typically described with the aid of a dimensionless parameter r_s, which is the radius of the average volume for a conduction electron in

atomic units. The Fermi momentum p_F is directly related to r_s. By varying the free electron density, the change in p_F due to a change in r_s is accompanied by a change in the strength of the electron-electron interaction. Changing the temperature does introduce similar but weaker effects, but the electron-ion interaction is also affected [134]. The theoretical predictions on the strength and detailed dependencies of the effects of electron correlation are quite mixed [125]. An experiment on the same solid-state system with varying the free electron density without any major changes in the atomic structure is required to separate the effects arising from changes in the free electron density from the solid-state effects. Only a few experiments have been done so far to access the different free electron densities, but only with different elements [135]. According to the results obtained, the general behavior of the free electron gas is in excellent agreement with the theoretical model based on the random-phase approximation [136].

6 Applications on Novel Materials

The advances gained in the experimental procedures to ensure the high quality of the acquired data were utilized in two new IXS experiments. Both studies were conducted utilizing the scanning crystal spectrometer at the beamline ID15B, ESRF (Section 3.4.1) [85]. The excellent properties of the spectrometer, i.e. high-precision monitoring, well-defined efficiency characterization and automated data acquisition, coupled to the high stability of the ESRF synchrotron source, allowed to reach the 0.1 % statistical accuracy level at the IXS profile peak for the directional differences.

The systems studied are novel complex materials, i.e. a high-T_C superconductor $La_{1.85}Sr_{0.15}CuO_4$ (Section 6.1) and a decagonal quasicrystal $Al_{0.72}Co_{0.17}Ni_{0.11}$ (Section 6.2). The reported theoretical studies on these compounds are very limited or even absent. For the time being, the yet unpublished experimental results presented here are waiting for the theoretical methods to achieve the level of accuracy accomplished. The detailed analysis and interpretation of the experimental results is thus still in progress. Also, the work to develop theoretical methods applicable to the quasicrystalline compounds has been started.

6.1 High-T_C Superconductors

6.1.1 Introduction

Since the discovery of the high-T_C superconductivity in rare-earth cuprate oxides [5], their electronic properties have been under intensive experimental and theoretical research. Several models have been proposed to explain their unique features [137], e.g. with the electron correlation effects [138], or with the electronic properties of the CuO_n (n = 2,5,6) blocks, and their mutual coupling to the layered crystal structure and to the antiferromagnetic spin ordering [139]. In particular, the hybridization of the Cu $3d$ states with the O $2p$ orbitals seems to be the common denominator to most of the models. The high-T_C materials are currently viewed as antiferromagnetic doped charge-transfer insulators [140]. The modern theoretical methods describe the overall features of the electronic structure of high-T_C superconductors quite well despite some discrepancies in the details. However, no consensus exists yet about which model is the correct one, nor do the theories have predictive value on a quantitative level, e.g. on the transition temperature on the basis of the structure and composition.

The electronic properties of the $La_{1.85}Sr_{0.15}CuO_4$ have been studied before utilizing several experimental methods, e.g. Raman-scattering [141], positron-annihilation technique [142], resonant X-ray fluorescence spectroscopy [143], (polarization dependent) X-ray absorption spectroscopy [144,145], and the various electron spectroscopy techniques [146]. Up to date, no high-resolution IXS studies have been reported.

IXS spectroscopy at large energy and momentum transfers is a very sensitive probe for the electronic ground-state properties of condensed matter systems [2,3, 47–49]. It is most sensitive to the interesting valence electron states because their contribution is confined to the peak area of the Compton profile due to the lower average momentum. Additionally, the interpretation of the acquired Compton spectrum is pretty straightforward due to the direct projective character of the process. However, the 1D Fourier transform of the directional Compton profiles (acquired with the scattering vector $\mathbf{q}$ along to a given crystal direction) does not give any direct structural information of the target in a general case [50] but a definite correlation between the electronic structure and the features found in the profiles or in the directional differences does exist [53,54].

The other experimental methods directly probing the electronic properties of matter, e.g. the positron-annihilation technique, (polarization dependent) X-ray absorption spectroscopy, X-ray fluorescence spectroscopy, and the various electron spectroscopy techniques [56] each have their pertinent strengths and weaknesses over the Compton scattering technique. They are essentially surface-sensitive techniques, or restricted to relatively thin samples. The high-energy X-rays, on the contrary, typically penetrate mm's or even up to cm's, probing the very bulk of the target. The Compton scattering technique is also quite insensitive to the crystal quality, unlike the methods utilizing electrons or positrons. The various X-ray absorption and fluorescescence techniques are, however, superior to IXS spectroscopy in some respect although the ground-state properties are inaccessible. They probe only the chosen electron states, with added capability to selectively utilize resonance and polarization sensitivity to enhance the detection of a given feature. For $La_{1.85}Sr_{0.15}CuO_4$, a nice example of this is the observation that the symmetry of the hybridized Cu $3d$ and O $2p$ states is predominantly of the planar type. Nevertheless, the full 3D momentum density can be reconstructed from the measured Compton profiles [53,57], or it can be acquired directly with the (γ,eγ) technique [58].

6.1.2 Electronic Structure

Upon doping the La_2CuO_4 (dielectric at room temperature) with Sr, La is partly displaced by Sr, turning the $La_{2-x}Sr_xCuO_4$ into a metallic conductor at room temperature. The atomic structure still remains body-centered tetragonal ($I4/mmm$) with lattice constants of $a = b = 3.78$ Å and $c = 13.22$ Å [147]. Below 180 K an orthorhombic distortion Abma exists which is essentially a formation of a new enlarged unit cell with $a' \sim \sqrt{2}\,a$, $b' \sim \sqrt{2}\,b$ and $c' \sim c$. Characteristic of the atomic structure is the considerably shorter Cu-O bond length of the planar oxygen (1.9 Å) compared to that of the apical oxygen (2.4 Å) which lies at a similar distance to the La (or Sr) opposite to the planar Cu.

Upon doping, the LaO-layers gain p-type characteristics [148] which is due to the dopant Sr^{2+} being less electronegative compared to the La^{3+}, thus attracting more holes. Thus, the CuO_2 planes become effectively n-type due to the requirement of charge conservation. Superconductivity is enabled for $0.05 \leq x \leq 0.30$ with the highest T_C of ~ 37 K for $x \simeq 0.15$ roughly. As the $La_{1.85}Sr_{0.15}CuO_4$ clearly is a p-type superconductor [148], the supercurrent flows in the charge-reservoir LaO-layers.

6.1.3 Theoretical Calculations

The theoretical computations were based on the all-electron charge self-consistent Korringa-Kohn-Rostoker methodology [149]. The exchange-correlation effects were incorporated within the von Barth-Hedin local density approximation [150]. Before the actual Compton profile calculations, the band structure problem was solved to a high degree of self-consistency. The energy bands, Fermi energy, and crystal potential converged to about 1 meV. Using the converged potential, the electronic structure wave functions were then obtained in over 1800 *ab initio* **k** points in the irreducible $1/16^{th}$ of the Brillouin zone. This basic data set allows for an efficient evaluation of the electronic momentum density $\rho(\mathbf{p})$ in a **p**-point grid extending to about 10 a.u.. Each **k**-point was translated via the reciprocal lattice vectors to obtain the $\rho(\mathbf{p})$ at 251 **p**-points.

The Compton profiles along the given directions were computed by integrating the $\rho(\mathbf{p})$ over a series of planes corresponding to different momentum transfers p_z along the surface normal. Care was necessary in carrying out the two-dimensional integrals since the $\rho(\mathbf{p})$ possesses sharp structures arising from the Fermi surface. For this purpose, a highly vectorized computer code applicable to general lattices was developed using the tetrahedral method of Lehmann and Taut [151]. The directional Compton profiles ([001] and [100]) for the La_2CuO_4 were obtained in a momentum mesh varying from 0.025 a.u. to 0.1 a.u. being accurate to a few parts in 10^3. The total number of valence electrons is reproduced correctly to one part in 10^3 by the theoretical Compton profiles over the range 0 – 10 a.u..

6.1.4 The Experiment

The alignment of the $La_{1.85}Sr_{0.15}CuO_4$ single crystal (grown in Tohoku University, Japan) was checked with the Laue method. The accuracy reached is enough for IXS spectroscopy because no sub-degree alignment accuracy is needed due to the projective nature of the IXS process. The relevant crystal directions were identified by comparing the exposed Laue pictures to the predicted figures from the *LaueX* package [153]. The alignment error was estimated 2 – 3 degrees at most. The Compton profiles for $La_{1.85}Sr_{0.15}CuO_4$ were acquired at room temperature in the directions [001] and [100] with the ID15B spectrometer [85] at a scattering angle

of 160°. Also the Ge solid-state detector at a scattering angle of 140° (utilized as a secondary monitor) was used for data acquisition. The individual scans took about one hour to complete, while the Ge spectra were saved and cleared every 15 minutes for reference. All the scans were used for the data analysis, as all the corrections due to the inescapable interrupts in the incident beam delivery could be made reliably thanks to the several beamline macros for automatization of the data acquisition. Incident energy of 58 keV was used in the experiment. For the elastic line, the obtained energy resolutions were 100 eV and 400 eV (for the scanning crystal spectrometer and the solid-state detector, respectively) corresponding to 0.17 and 0.55 a.u. at the Compton profile peak, respectively. After the standard procedures to apply the incident intensity normalization, spectrometer efficiency and absorption corrections and the conversion of the profiles to the p_z-scale with the differential correction, the background subtraction was done with the aid of the theoretical core profiles.

6.1.5 Discussion

The experimental anisotropy (Fig. 3) is essentially identical for both spectrometers within the momentum resolution and statistical errors. Yet, some of the features predicted by the calculation are clearly different. First, most of the anisotropy is confined to lower momentum transfers than expected, indicating a higher asymmetry of the valence electron states, e.g. due to hybridization. Secondly, the observed features are somewhat shifted upwards in momentum, and slightly weaker in amplitude. The same trend in the amplitude is observed for all the high-T_C superconductors [154]. The shift in momentum might be due to doping. The apical O_{Sr} experiences a less attractive electrostatic potential than the O_{La} due to the difference in the ionic charges (Sr^{2+} vs. La^{3+}). Thus, as the Fermi level is upon doping pushed into the valence band of the planar O $2p$ character predominantly, the spectral weight of the apical O $2p$ states close to Sr sites changes [145]. This would also explain the sensitivity of the density of states of the apical oxygen to doping while its effective charge remains practically constant [148]. Further, the signatures of the Fermi surface are weaker than anticipated. A sharp Fermi surface originates from a high degree of long-range order in the periodic ion potential, a condition which is broken with doping, leading to increased smearing of the Fermi surface. In spite of that, the experiments on nearly defect-free single crystals of La_2CuO_4 performed with positrons have shown that no discernible Fermi surface structures exist at the Brillouin zone boundaries [142]. Also, discrepancies in the peak locations have been observed, in agreement with the results presented here. A more careful analysis together with new theoretical calculations is in progress.

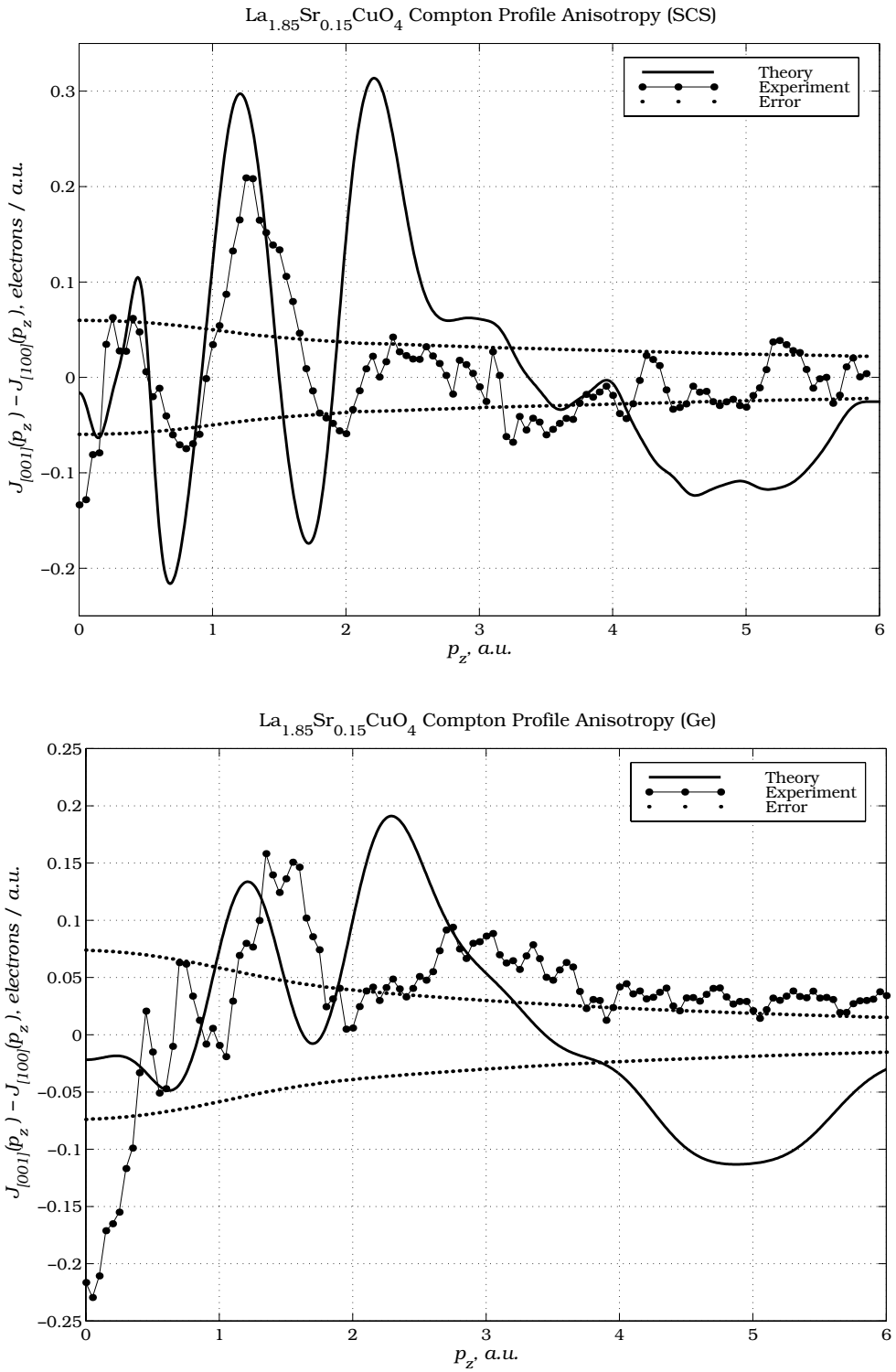

Fig. 3. The Compton profile anisotropies for the high-T_C superconductor $La_{1.85}Sr_{0.15}CuO_4$ between the crystal directions [001] and [100], and the results of the KKR-calculation for La_2CuO_4. Both the high-resolution spectrometer (SCS) and a conventional solid-state spectrometer (Ge) were used.

6.2 Quasicrystals

6.2.1 Introduction

The discovery of quasicrystals [6] in rapidly quenched binary alloys [7] implied an entirely new type of structural ordering for solid-state matter, additional to the previously known forms i.e. crystalline, distorted and amorphous matter. The quasicrystal lattices possess quasi-periodic translational (bond-orientational) long-range order in 3D space, associated to non-crystallographic rotational symmetry axes, which is explicitly incompatible with the classic Bravais lattices. Yet, quasicrystals do have well-defined discrete crystallographic point groups, e.g. in 5D space [155]. The first quasicrystal structures were disordered to a significant degree, hampering the detection of the properties intrinsic to the quasi-periodicity. The thermodynamically stable quasicrystals discovered later possess a very high degree of structural perfection, comparable to that in the best periodic alloys.

Both the physical and electrical properties of quasicrystals are very similar to the corresponding crystalline or amorphous counterparts, depending on the lattice symmetry and direction [156,157]. Qualities reminiscent of metallic, semimetallic, semiconducting, and even dielectric behavior are found. Still, the theoretical studies on the detailed electronic structure of quasicrystals meet severe difficulties. The non-periodicity can be overcome only partly by utilizing so-called crystalline approximants or periodic average structures [155,158–161], which are perfectly periodic crystal structures in 3D space consisting typically of 10 – 1000 atoms and locally resembling the quasicrystalline atomic structure in a satisfactory way. On a qualitative level, the electronic structure of quasicrystals is understood adequately. The progress has been significantly slower on the quantitative level due to the practical difficulties encountered in the calculations. Furthermore, the lack of accurate results obtained with the direct-probing experimental methods, e.g. X-ray spectroscopy or the positron-annihilation technique, has hindered the development.

Decagonal quasicrystals [157] combine the structural features of both the crystalline and the quasicrystalline systems. The quasi-periodically ordered layers are stacked with perfect translational periodicity, thus exhibiting a quite unconventional anisotropy both for the structure and for the electronic properties. Decagonal systems are expected to exhibit a greater degree of anisotropy in electronic structure than the icosahedral systems which are completely quasi-periodic in 3D, due to which they are often called 'true quasicrystals'. Indeed, remarkable anisotropies of electrical and thermal transport, optical conductivity and the Hall-effect have been established [162,163], indicative of an anisotropic Fermi surface. One of the first stable decagonal quasicrystal structures found was formed in the ternary Al-Co-Ni alloy system (5D crystallographic point group $P10_5/mmc$) [164], for which the monoclinic binary alloy $Al_{13}Co_4$ is considered the best approximant.

Both the Compton and the positron-annihilation techniques have been used previously to examine the electronic properties of the icosahedral quasicrystals [165–167]. In the first IXS experiment [165], no anisotropy between the directions corresponding to the 5-fold and 2-fold symmetry axes was observed because of the limited uniformity of 0.5 % in the detection efficiency of the image plates used as the detector. The positron-annihilation results [166] suffered from sample imperfections. The combined study [167] showed some signs of an anisotropy in the value of the Fermi momentum but the results were not explicit within the experimental errors. Further, inelastic neutron scattering has been applied to study the lattice dynamics [168]. These results serve nicely to highlight the subtlety of the effects being sought. With IXS care must be taken to achieve the desired resolution as well as good enough counting statistics.

6.2.2 Electronic Structure

Despite the remarkable peculiarities, quasicrystals are still clearly metallic in character, suggesting the existence of a well-defined Fermi surface [156,157,162,163, 169]. Due to their distinctive higher-dimensional point symmetry, the quasi-Brillouin zone-boundary comprimizes several tens of facets, allowing for close matching of the nearly spherical Fermi surface with the zone boundary. As a result, most of the Fermi surface is thought to be obliterated. The only fragments expected to survive are small electron- and hole-pockets at the facet centers and corners, respectively. The so-called many-pocketed electronic structure should manifest itself via a highly spiky density of states in the vicinity of the E_F. However, the quasicrystal systems do differ strikingly in this respect.

The icosahedral quasicrystals possess the highest point-symmetry which has been exploited by theories considering band-structure effects to explain some of their properties [156,169]. The prominent pseudo-gap predicted was also found experimentally [156,170] but it should be absent in the decagonal systems [171]. However, the theoretical results are very sensitive to the specifics of the model employed. One feature common to many of these efforts to study the decagonal systems is the importance of hybridization of the transition-metal d-states with the Al s- and p-states [159,161], which leads to a lower density of states at the E_F. So the pseudogap, if it exists, might be unrelated to the symmetry of the structure. Closely associated to this, the decagonal systems also exhibit relatively small electronic contribution to the specific heat due to the reduced density of states at the E_F [163].

6.2.3 The Experiment

The inelastic X-ray scattering study on a high-quality single-grain flux-grown [172] decagonal quasicrystal $Al_{0.72}Co_{0.17}Ni_{0.11}$ was conducted utilizing the high-resolution

crystal spectrometer at the beamline ID15B (ESRF, France) (Section 3.4.1) [85]. The crystal was cut and polished into a rectangular parallelepiped with dimensions $x = 7$ mm, $y = 1.5$ mm, and $z = 1.5$ mm, with x and y parallel to the 2-fold P- (facet edges) and D-axes (facet centers), respectively, and z parallel to the decagonal c-axis. Transmission electron diffraction from a small slice cut from the sample confirmed the y direction as the D-axis. A mosaic spread of only 0.14 % in the 2-fold directions was observed with X-ray diffraction rocking curve scans, indicating very high sample quality. The exact composition was determined with quantitative electron probe microanalysis. The sample consisted of the 'basic Co-rich' phase, consistent with the atomic composition.

The spectrometer was utilized at a scattering angle of 173 degrees with an incident energy of 58 keV, and incident beam size of 4.6 mm (V) $\times$ 0.2 mm (H), and an energy resolution of about 100 eV at the elastic line, corresponding to a momentum resolution of 0.17 a.u. at the Compton peak. The Compton scattering spectra, i.e. the projections of the 3D electronic momentum density onto the scattering vector p_z, were acquired in air in the primary 2-fold (P-axis), 10-fold and three other quasicrystallographic directions of interest with a statistics of better than 0.1 % at the profile peak. Each directional profile was scanned in several successive runs, taking about one hour to complete. Several beamline macros were utilized during the experiment to automatize the data acquisition process due to unavoidable interrupts in the beam delivery. They enabled to use all the obtained scans in the analysis as all the corrections to the acquired spectra could be made in a reliable way.

The acquired spectra were checked and normalized with the information obtained from the incident beam intensity monitor. The integrity of this monitor was examined against a secondary monitor used for the scattered radiation (a Ge solid-state detector), and no incompatibilities were found. The spectrometer geometry and efficiency corrections as well as the absorption corrections were applied to the error weighted average of the time normalized spectra. Conversion to the momentum scale p_z was applied following Holm's relativistic approach [13] including the differential correction. Both the acquired experimental background and the theoretical core profiles, corrected for the effects due to the failure of the impulse approximation [44], were utilized in the background subtraction. The multiple scattering correction was calculated with an optimized Monte-Carlo method [115]. Finally, the spectra were normalized according to the number of electrons and the error weighted averages of the low- and high-energy sides of the profiles were computed. As the Compton profiles itself are not the most informative way to look at the properties of the electronic momentum distribution, the directional anisotropies were calculated, providing a more convenient and reliable way to find the relevant features.

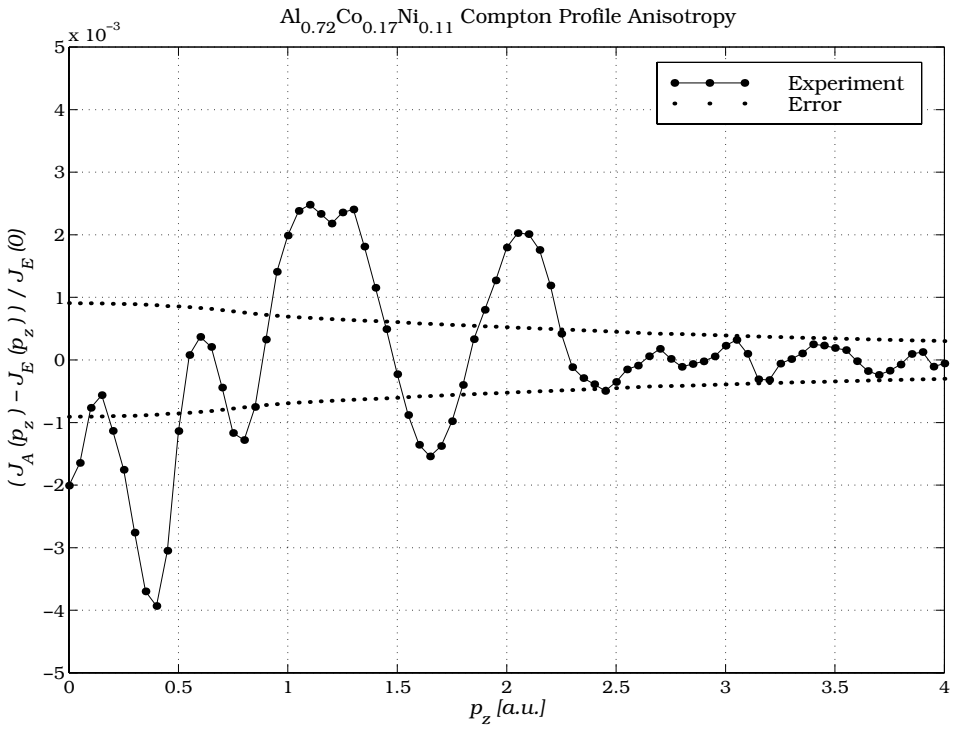

Fig. 4. The experimental directional Compton anisotropy for the decagonal quasicrystal $Al_{0.72}Co_{0.17}Ni_{0.11}$ between the crystal directions of 10-fold [0000 1] and 2-fold [1000 0] symmetry. A clear anisotropy is observed.

6.2.4 Discussion

Direct evidence for an anisotropy in the electronic momentum density in quasicrystals is observed for the first time. The magnitude of the anisotropy is 0.4 % maximum, which is below the accuracy limits of the previous experiments. Further, the numerous distinct features broader than the experimental resolution of 0.17 a.u. are taken indicative of the more detailed structure of the Fermi surface. The many-pocketed picture of the Fermi surface is clearly supported. A clear low-momentum deficiency is observed in the direction(s) where the hole-pockets should reside. Further, the unique structural anisotropy modifies the electronic momentum density to a significant degree. Sharp Fermi surface signatures originate from a periodic momentum distribution over large distances in a periodic lattice. For the $Al_{0.72}Co_{0.17}Ni_{0.11}$, this is valid in the 10-fold direction only while the 2-fold directions are quasi-periodic. Thus, the spectral weight of the electron momentum density near the Fermi level is dependent on the crystal direction. Nevertheless, the resulting effects in the directional anisotropies are easily seen. However, as no theoretical calculations on the exact electronic structure of decagonal quasicrystals for comparison currently exist, the interpretation of the experimental result is not that straightforward.

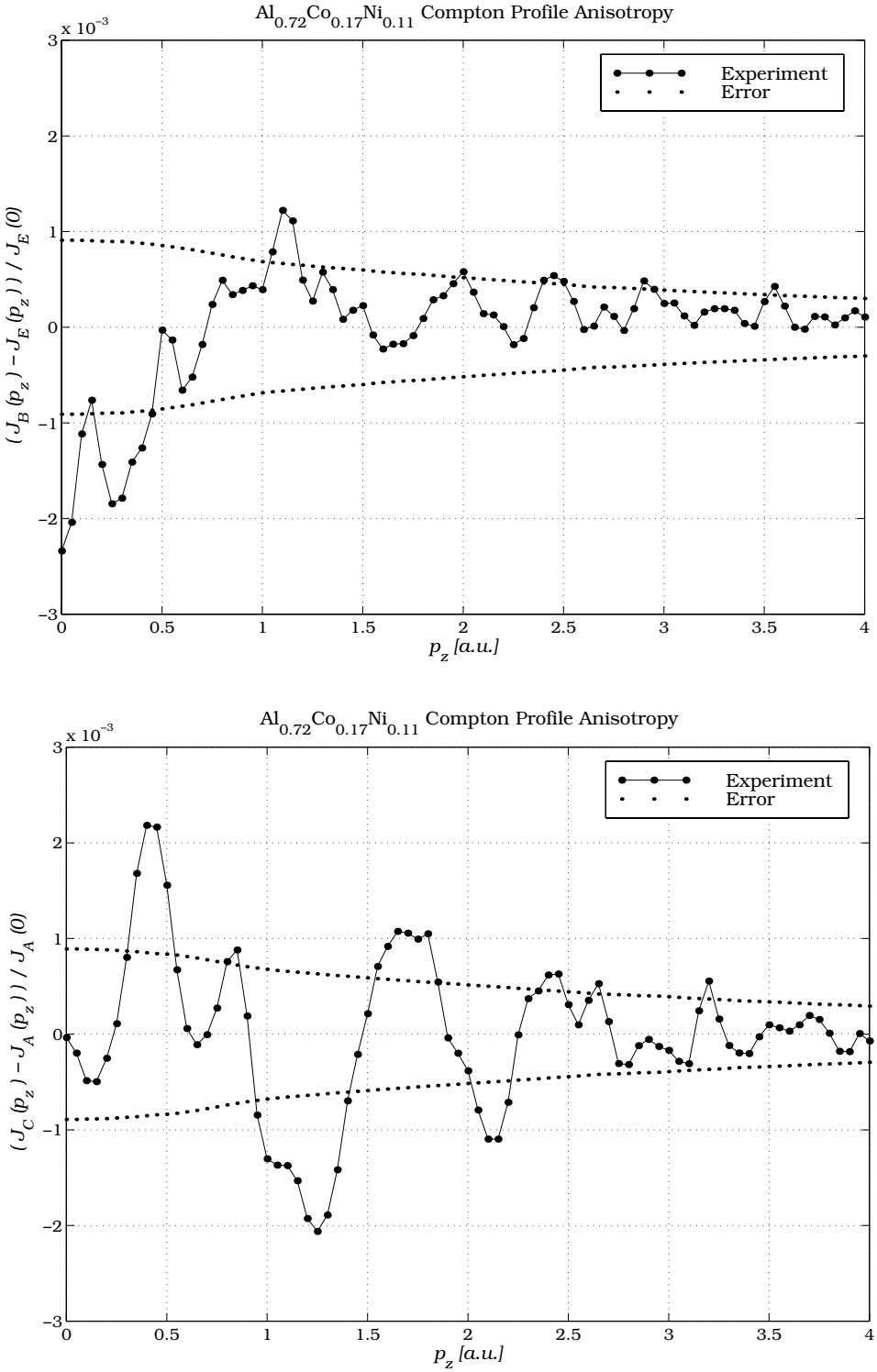

Fig. 5. The experimental directional IXS anisotropies for the decagonal quasicrystal $Al_{0.72}Co_{0.17}Ni_{0.11}$ between the crystal directions of 30° off the 10-fold direction (hole-pockets in the Fermi surface expected) and the [1000 0], and 10-fold axis [0000 1] and 30° off the 2-fold axis. In the first case, a clear low-momentum deficiency is found. For the latter case, electron-pockets are expected in both directions but the unique structural anisotropy modifies the electronic momentum density to a significant degree.

7 Summary of the Published Papers

The papers included in this thesis involve applications of IXS spectroscopy to various issues in solid-state physics. The principal aspects of the work lie in the experimental techniques. Several improvements to the key procedures and measurement systems have been introduced on the course of the work. The advances have enabled some experimental discoveries that are either supported by the latest theoretical results or still need more development on the physical models.

Paper I reports the first user experiments with the high-resolution scanning crystal spectrometer installed at the beamline ID15B at the European Synchrotron Radiation Facility, France. The effects due to the structure of the Fermi surface to the Compton profiles and to the directional anisotropies could be reliably seen due to the high momentum resolution of the spectrometer. The very recently developed model utilized to interpret the result successfully explained a significant part of the observed effects to originate from a single partly-filled electron shell.

Paper II introduces a novel detector collimation scheme together with a compact scattering geometry, and a modified fast-slow coincidence electronics system to enhance the counting performance of the entire acquisition system. The absolute double-differential IXS cross-section for the Cu K-shell electrons is determined for three momentum transfer values in the intermediate transfer range. No suggested resonant structures were found. Instead, the impulse approximation was found to work significantly better than expected. The small deviations are explained by a more detailed quantum-mechanical calculation.

Paper III is an extension to the previous work. The experimental advances gained were utilized to demonstrate the feasibility of the technique in a modern third generation synchrotron source. A procedure to optimize the several experimental factors relevant to the statistical accuracy of the given coincidence experiment was developed. The employed scheme enabled to achieve a true-to-chance coincidence ratio similar to that previously attained only with conventional radiation sources.

Paper IV presents the details of the first successfull high-pressure IXS experiment. The effects in the properties of the Compton profile due to the varying electron-electron correlation induced by the changing free electron density were demonstrated. The free electron density was changed directly by applying a variable high pressure to the sample. The changes observed in the profiles are described quite well by a model based on the random-phase approximation.

8 Conclusions

Inelastic X-ray scattering is a very powerful technique in condensed matter research. When applied utilizing modern experimental high-accuracy apparatus, it provides valuable information on the behavior of the electronic systems under study. However, thorough understanding of the factors affecting the quality and accuracy of the experiments is needed. Otherwise, the results may be misinterpreted only due to experimental artifacts, not necessarily having any direct relation to the physics of the target system.

The improvements introduced to the coincidence technique allowed for the first time a direct meaningful comparison with theory. Also, it was conclusively shown that the technique is feasible on third generation synchrotron sources, contrary to some previous opinions. The advantages of the crystal spectrometers in IXS spectroscopy were proven earlier by the pioneers in the field. However, the reproducibility and applicability of the technique down to a 0.1 % accuracy level on a variable intensity radiation source is certainly not self-evident. A well-designed, properly operated and monitored spectrometer will render the acquisition of tens of IXS spectra sequentially possible with high enough consistency and accuracy.

Yet, plenty of room for development still exists. A similar coincidence experiment to that of **Paper II** on a synchrotron source with a crystal spectrometer would reveal whether the profile truly is featureless in terms of any additional structures to that of the smooth IXS core profile itself. Further, according to some proposals the result would be quite different for the L-shell electrons, i.e. the profile should pose some extra features. This would be very interesting but also very hard to test.

The discovery of the directional anisotropy in the electron momentum density of the decagonal quasicrystals left a question unanswered: is the anisotropy unique for the decagonal systems due to their layered structure, or are the icosahedral systems similar in this respect? The answer might provide some important clues on the key features of the electronic properties of quasicrystals. However, until the theoretical methods improve considerably, no decisive conclusions on the most relevant features of the electronic structure of the novel materials concerning their electronic properties can be done. The author's work on this issue will continue.

References

[1] A. H. Compton, *Phys. Rev.* **21** (1923) 484; *ibid.* **22** (1923) 409

[2] M. J. Cooper, *Rep. Prog. Phys.* **48** (1985) 643

[3] P. P. Kane, *Phys. Rep.* **218** (1992) 67; *Radiat. Phys. Chem.* **50** (1997) 31

[4] *Handbook on Synchrotron Radiation*, Volumes 1A & 1B, edited by E.-E. Koch, North-Holland (1983); Volume 2, edited by G. V. Marr, North-Holland (1987); Volume 3, edited by G. S. Brown and D. E. Moncton, North-Holland (1991); Volume 4, edited by S. Ebashi, M. Koch and E. Rubenstein, North-Holland (1991); *Synchrotron Radiation Research*, Volumes 1 & 2, edited by R. Z. Bachrach, Plenum (1992)

[5] J. G. Bednorz and K. A. Müller, *Z. Phys. B* **64** (1986) 189

[6] D. Levine and P. J. Steinhardt, *Phys. Rev. B* **34** (1986) 596; J. E. S. Socolar and P. J. Steinhardt, *ibid.* 617

[7] D. Shechtmann, I. Blech, D. Gratias and J. W. Kahn, *Phys. Rev. Lett.* **53** (1984) 1951; D. Levine and P. J. Steinhardt, *ibid.* 2477; L. Bendersky, *Phys. Rev. Lett.* **55** (1985) 1461

[8] J. M. Jauch and F. Rohrlich, *The Theory of Photons and Electrons*, Addison-Wesley (1955)

[9] P. M. Platzman, and N. Tzoar, in *Compton Scattering*, edited by B. Williams, McGraw-Hill (1977)

[10] M. Weissbluth, *Atoms and Molecules*, Academic Press (1978)

[11] F. Bassani and M. Altarelli, in *Handbook on Synchrotron Radiation*, Volume 1A, edited by E.-E. Koch, North-Holland (1983)

[12] W. Schülke, in *Handbook on Synchrotron Radiation*, Volume 3, edited by G. S. Brown and D. E. Moncton, North-Holland (1991)

[13] P. Holm, *Phys. Rev. A* **8** (1988) 3706

[14] E. Bürkel, *Rep. Prog. Phys.* **63** (2000) 171

[15] H. A. Kramers and W. Heisenberg, *Z. Phys.* **31** (1925) 681

[16] J. J. Thomson, *Electricity and Matter*, New Haven, USA (1904)

[17] O. Klein and Y. Nishina, *Zeits. für Phys.* **52** (1929) 853; I. Tamm, *Zeits. für Phys.* **62** (1930) 545

[18] S. Manninen, *Radiat. Phys. Chem.* **50** (1997) 77

[19] K. Das Gupta, *Phys. Rev. Lett.* **3** (1959) 38

[20] C. J. Sparks Jr., *Phys. Rev. Lett.* **33** (1974) 262

[21] M. Gavrila and M.N. Tugulea, *Rev. Roum. Phys.* **20** (1975) 209

[22] P. M. Platzman, *Phys. Rev. B* **40** (1989) 5883; P. M. Platzman and E. D. Isaacs, *Phys. Rev. B* **57** (1998) 11107

[23] J. P. Briand, D. Girard, V. Kostroun, P. Chevallier, K. Wohrer and J. P. Mosse, *Phys. Rev. Lett.* **46** (1981) 1625; J. P. Briand, A. Simionovici, P. Chevallier and P. Indelicato, *Phys. Rev. Lett.* **62** (1989) 2092; A. Simionovici, J. P. Briand, P. Indelicato and P. Chevallier, *Phys. Rev. A* **41** (1990) 3707

[24] Y. Ma, *Phys. Rev. B* **49** (1994) 5799

[25] P. M. Platzman and N. Tzoar, *Phys. Rev.* **2A** (1965) 410; P. Eisenberger and P. M. Platzman, *Phys. Rev. A* **2** (1970) 415; P. Eisenberger and W. A. Reed, *Phys. Rev. B* **9** (1974) 3237

[26] S. Manninen, T. Paakkari and K. Kajantie, *Phil. Mag.* **29** (1974) 167

[27] R. Ribberfors, *Phys. Rev. B* **12** (1975) 2067; *ibid.* 3136

[28] M. Gavrila, *Lett. Nuovo Cimento* **5** (1969); *Phys. Rev. A* **6** (1972) 1348; *ibid.* 1360; *Rev. Roum. Phys.* **19** (1974) 473

[29] G. C. Spitale and S. D. Bloom, *Phys. Rev. A* **16** (1977) 221; G. Basavaraju, P. P. Kane and S. M. George, *Phys. Rev. A* **36** (1987) 655

[30] V. Marchetti and C. Franck, *Phys. Rev. Lett.* **59** (1987) 1557; *Rev. Sci. Instrum.* **59** (1988) 407; *Phys. Rev. A* **39** (1989) 647

[31] S. Manninen, K. Hämäläinen and J. Graeffe, *Phys. Rev. B* **41** (1990) 1224

[32] T. Surić, P. M. Bergstrom Jr., K. Pisk and R. H. Pratt, *Phys. Rev. Lett.* **67** (1991) 189; P. M. Bergstrom Jr., T. Surić, K. Pisk and R. H. Pratt, *Phys. Rev. A* **48** (1993) 1134

[33] K. Namikawa and S. Hosoya, *Phys. Rev. Lett.* **53** (1984) 1606

[34] S. Satō and Y. Ohmura, *Phys. Rev. B* **43** (1991) 12246

[35] P. Froelich and W. Weyrich, *J. Chem. Phys.* **80** (1984) 5669; P. Froelich, A. Flores-Riveros and W. Weyrich, *J. Chem. Phys.* **82** (1985) 2305; P. Froelich and W. Weyrich, *J. Chem. Phys.* **85** (1986) 1456

[36] C. Sternemann, K. Hämäläinen, A. Kaprolat, A. Soininen, G. Döring, C.-C. Kao, S. Manninen and W. Schülke, Submitted to *Phys. Rev. Lett.* ; S. Huotari, K. Hämäläinen, S. Manninen, S. Kaprzyk, A. Bansil, W. Caliebe, T. Buslaps, V. Honkimäki and P. Suortti, Submitted to *Phys. Rev. B*

[37] R. J. Weiss, *Phil. Mag.* **32** (1975) 247; R. J. Weiss, M. J. Cooper and R. S. Holt, *Phil. Mag.* **36** (1977) 193; P. Pattison and S. Manninen, *ibid.* 1265; R. S. Holt, *Phil. Mag.* **39** (1979) 541

[38] A. D. Barlas, W. H. E. Rückner and H. F. Wellenstein, *Phil. Mag.* **36** (1977) 201; W. H. E. Rückner, A. D. Barlas and H. F. Wellenstein, *Phys. Rev. A* **18** (1978) 895; A. D. Barlas, W. H. E. Rückner and H. F. Wellenstein, *J. Phys. B* **11** (1978) 3381

[39] A. Lahman-Bennani, A. Duguet and H. F. Wellenstein, *Chem. Phys. Lett.* **60** (1979) 411; A. Lahman-Bennani, A. Duguet, H. F. Wellenstein and M. Rouault, *Chem. Phys. Lett.* **72** (1980) 6398; A. Lahman-Bennani and A. Duguet, *Chem. Phys. Lett.* **74** (1980) 85; A. Lahman-Bennani, A. Duguet and M. Rouault, *Chem. Phys. Lett.* **78** (1983) 1838

[40] T. C. Wong, L. B. Mendelson, H. Grossman and H. F. Wellenstein, *Phys. Rev. A* **26** (1982) 181; C. Tavard, M. C. Dal Cappello, F. Gasser, C. Dal Cappello and H. F. Wellenstein, *Phys. Rev. A* **27** (1983) 199

[41] L. B. Mendelsohn and H. Grossman, *AIP Conference Proceedings* **36** (1977) 249 I. E. McCarthy and R. A. Bonham, *ibid.* 255

[42] F. Gasser and C. Tavard, *Chem. Phys. Lett.* **79** (1981) 97; F. Gasser and C. Tavard, *Phys. Rev. A* **27** (1983) 117; F. Gasser and M. Roeth, *Z. Naturforsch.* **48A** (1993) 257

[43] F. Bell, *J. Chem. Phys.* **85** (1986) 303

[44] P. Holm and R. Ribberfors, *Phys. Rev. A* **40** (1989) 6251

[45] J. W. H. Dumond, *Phys. Rev.* **33** (1929) 643; *ibid.* **36** (1930) 146

[46] P. Eisenberger and W. A. Reed, *Phys. Rev. A* **5** (1972) 2085; W. A. Reed and P. Eisenberger, *Phys. Rev. B* **6** (1972) 4596

[47] L. Dobrzyński, *Z. Naturforsch.* **48A** (1993) 266

[48] E. Isaacs and P. Platzman, *Physics Today* **49**, No. 2 (1996) 40

[49] K. Hämäläinen, S. Manninen, W. A. O. L. Caliebe, C.-C. Kao and J. B. Hastings, *AIP Conference Proceedings* **389** (1997) 671; S. Manninen, *J. Phys. Chem. Solids* **61** (2000) 335

[50] W. Schülke, *Phys. Status Solidi B* **82** (1977) 229

[51] T. Paakkari and V. Halonen, *Physica Scripta* **17** (1978) 433; T. Paakkari, *Chem. Phys. Lett.* **55** (1978) 160; O. Aikala, *Solid State Comm.* **32** (1979) 699; B. L. Ahuja, B. K. Sharma and O. Aikala, *Pramana* **29** (1987) 313; K. Mansikka and O. Aikala, *Physica Scripta* **37** (1988) 816

[52] T. Paakkari and S. Manninen, *Solid State Comm.* **38** (1981) 787; O. Aikala, T. Paakkari and S. Manninen, *Acta Cryst. A* **38** (1982) 155; B. K. Sharma, S. Manninen, T. Paakkari, M. W. Richardson and S. Rundqvist, *Phil. Mag. B* **49** (1984) 363; S. Manninen, T. Paakkari, B. K. Sharma and M. W. Richardson, *Ind. J. Phys. A* **59** (1985) 389; R. Benedek, R. Prasad, S. Manninen, B. K. Sharma, A. Bansil and P. E. Mijnarends, *Phys. Rev. B* **32** (1985) 7650; S. Perkkiö, S. Manninen and T. Paakkari, *Phys. Rev. B* **40** (1989) 8446

[53] Y. Tanaka, N. Sakai, Y. Kubo and H. Kawata, *Phys. Rev. Lett.* **70** (1993) 1537; K. Hämäläinen, S. Manninen, C.-C. Kao, W. Caliebe, J. B. Hastings, A. Bansil, S. Kaprzyk and P. M. Platzman, *Phys. Rev. B* **54** (1996) 5453; R. K. Pandya, K. B. Joshi, R. Jain, B. L. Ahuja and B. K. Sharma, *Phys. Status Solidi B* **200** (1997) 137; M. Marangolo, J. Moscovici, G. Loupias, S. Rabii, S. C. Erwin, C. Hérold, J. F. Marêché and P. Lagrange, *Phys. Rev. B* **58** (1998) 7593; A. Bansil, S. Kaprzyk, A. Andrejczuk, L. Dobrzyński, J. Kwiatkowska, F. Maniawski and E. Żukowski, *Phys. Rev. B* **57** (1998) 314; B. Králik, P. Delaney and S. G. Louie, *Phys. Rev. Lett.* **80** (1998) 4253; M. Itou, Y. Sakurai, T. Ohata, A. Bansil, S. Kaprzyk, Y. Tanaka, H. Kawata and N. Shiotani, *J. Phys. Chem. Solids* **59** (1998) 99

[54] C. Filippi and D. M. Ceperley, *Phys. Rev. B* **59** (1999) 7907; G. Stutz, F. Wohlert, A. Kaprolat, W. Schülke, Y. Sakurai, Y, Tanaka, M. Ito, H. Kawata, N. Shiotani, S. Kaprzyk and A. Bansil, *Phys. Rev. B* **60** (1999) 7099; E. D. Isaacs, A. Shukla, P. M. Platzman, D. R. Hamann, B. Barbiellini and C. A. Tulk, *Phys. Rev. Lett.* **82** (1999) 600; K. B. Joshi, R. Jain, R. K. Pandya, B. L. Ahuja and B. K. Sharma, *J. Chem. Phys.* **111** (1999) 163; S. Ishibashi, A. A. Manuel, D. Vasumathi, A. Shukla, P. Suortti, M. Kohyama and K. Bechgaard, *J. Phys.: Condens. Matter* **11** (1999) 9025; Y. Sakurai, S. Kaprzyk, A. Bansil, Y. Tanaka, G. Stutz, H. Kawata and N. Shiotani, *J. Phys. Chem. Solids* **60** (1999) 905; A. Andrejczuk, H. Reniewicz, L. Dobrzyński, E. Żukowski and S. Kaprzyk, *Phys. Status Solidi* **217** (2000) 903; See also *J. Phys. Chem. Solids* **61** Vol. 3 (2000)

[55] P. E. Mijnarends and A. Bansil, in *Positron Spectroscopy of Solids*, edited by A. Dupasquier and A. P. Mills, International School of Physics 'Enrico Fermi' (1995) 257

[56] W. E. Spicer, *J. Phys. Chem. Solids* **59** (1998) 527

[57] J.-M. Gillet, P. J. Becker and G. Loupias, *Acta Cryst. A* **51** (1995) 405; J.-M. Gillet, C. Fluteaux and P. J. Becker, *Phys. Rev. B* **60** (1999) 2345; G. Kontrym-Sznajd and M. Samsel-Czekala, *Appl. Phys. A* **70** (2000) 89

[58] C. Metz, T. Tschentscher, P. Suortti, A. S. Kheifets, D. R. Lun, T. Sattler, J. R. Schneider and F. Bell, *Phys. Rev. B* **59** (1999) 10512; C. Metz, T. Tschentscher, P. Suortti, A. S. Kheifets, D. R. Lun, T. Sattler, J. R. Schneider and F. Bell, *J. Phys.: Condens. Matter* **11** (1999) 3933

[59] I. E. McCarthy and E. Weigold, *Rep. Prog. Phys.* **54** (1991) 789; I. E. McCarthy, *Nucleus* **37** (1997) 181; I. E. McCarthy, *Austr. J. Phys.* **51** (1998) 593

[60] M. A. Coplan, J. H. Moore and J. A. Tossell *Z. Naturforsch.* **48A** (1993) 358; E. Weigold, *Z. Naturforsch.* **48A** (1993) 371

[61] I. E. McCarthy, *Z. Phys. D.* **23** (1992) 287

[62] P. Eisenberger and N. Tzoar, *Phys. Rev. B* **2** (1970) 3556

[63] N. Sakai and K. Ono *Phys. Rev. Lett.* **37** (1976) 351; *J. Phys. Soc. Jpn.* **42** (1977) 770

[64] R. S. Holt and M. J. Cooper, *Phil. Mag.* **41** (1981) 117; R. S. Holt, D. Laundy, D. A. Cardwell, M. J. Cooper, T. Naylor, S. Manninen and P. Hatton, *Nucl. Instr. and Meth. A* **243** (1986) 608; M. J. Cooper, D. Laundy, D. A. Cardwell, D. N. Timms, R. S. Holt and G. Clark, *Phys. Rev. B* **34** (1986) 5984

[65] N. Sakai, *AIP Conference Proceedings* **215** (1990) 749; *J. Appl. Cryst.* **29** (1996) 81; N. Sakai, A. Koizumi, N. Miyamoto and Y. Tanaka, *AIP Conference Proceedings* **389** (1997) 399

[66] D. B. McWhan, *J. Synchr. Rad.* **1** (1994) 83

[67] M. J. Cooper, S. P. Collins, S. W. Lovesey, D. Laundy and D. N. Timms, *Phys. Scr.* **T35** (1991) 103

[68] J. E. McCarthy, M. J. Cooper, P. K. Lawson, D. N. Timms, S. Manninen, K. Hämäläinen and P. Suortti, *J. Synchr. Rad.* **4** (1997) 102

[69] M. A. G. Dixon, J. A. Duffy, S. Gardelis, J. E. McCarthy, M. J. Cooper, S. B. Dugdale, T. Jarlborg and D. N. Timms, *J. Phys.: Condens. Matter* **10** (1998) 2759

[70] J. A. Duffy, J. E. McCarthy, S. B. Dugdale, V. Honkimäki, M. J. Cooper, M. A. Alam, T. Jarlborg and S. B. Palmer, *J. Phys.: Condens. Matter* **10** (1998) 10391

[71] N. Sakai, N. Shiotani, M. Ito,F. Itoh, H. Kawata, Y. Amemiya, M. Ando, S. Yamamoto and H. Kitamura, *Rev. Sci. Instrum.* **60** (1989) 1666; N. Sakai, M. Ito, H. Kawata, T. Iwazumi, M. Ando, N. Shiotani, F. Itoh, Y. Sakurai and S. Nanao, *Nucl. Instr. and Meth. A* **303** (1991) 488; Y. Tanaka, N. Sakai, H. Kawata and T. Iwazumi, *Rev. Sci. Instrum.* **63** (1992) 1213

[72] J. E. McCarthy, M. J. Cooper, V. Honkimäki, T. Tschentscher, P. Suortti, S. Gardelis, K. Hämäläinen, S. Manninen and D. N. Timms, *Nucl. Instr. and Meth. A* **401** (1997) 463; T. Tschentscher, J. E. McCarthy, V. Honkimäki and P. Suortti, *J. Synchr. Rad.* **5** (1998) 940

[73] S. W. Lovesey, *Phys. Scr.* **44** (1991) 51; *Rep. Prog. Phys.* **56** (1993) 257; *Z. Naturforsch.* **48A** (1993) 261; S. P. Collins, M. J. Cooper, S. W. Lovesey and D. Laundy, *J. Phys.: Condens. Matter* **5** (1990) 6439

[74] M. J. Cooper, E. Zukowski, S. P. Collins, D. N. Timms, F. Itoh and H. Sakurai, *J. Phys.: Condens. Matter* **4** (1992) 399; D. N. Timms, E. Zukowski, M. J. Cooper, D. Laundy S. P. Collins, F. Itoh, H. Sakurai, T. Iwazumi, H. Kawata, M. Ito, N. Sakai and Y. Tanaka, *J. Phys. Soc. Jpn.* **62** (1993) 1716; E. Zukowski, S. P. Collins, M. J. Cooper, D. N. Timms, M. Ito, H. Sakurai, H. Kawata, Y. Tanaka and A. Malinowski, *J. Phys.: Condens. Matter* **5** (1993) 4077

[75] P. Carra, M. Fabrizio, G. Santoro and B. T. Thole, *Phys. Rev. B* **53** (1996) 5994

[76] F. R. Elder, A. M. Gurewitsch, R. V. Langmuir and H. C. Pollock, *Phys. Rev.* **71** (1947) 829

[77] D. H. Tomboulian and P. L. Hartman *Phys. Rev.* **102** (1956) 1423

[78] J. D. Jackson, *Classical Electrodynamics*, John Wiley & Sons (1962); L. Landau and E. Lifchitz, *Théorie du Champ*, MIR, Moscow, USSR (1966)

[79] G. Margaritondo, *Introduction to Synchtrotron Radiation*, Oxford (1988); G. Margaritondo, *J. Synchr. Rad.* **2** (1995) 148

[80] P. M. Platzman, *Jap. J. Appl. Phys.* **17** (1978) 56

[81] G. Loupias and J. Petiau, *J. Phys. (Paris)* **41** (1980) 265

[82] W. Schülke, *Nucl. Instr. and Meth. A* **246** (1986) 491

[83] J. R. Schmitz, H. Schulte-Schrepping, A. Berthold, S. Mourikis and W. Schülke, *Nucl. Instr. and Meth. A* **317** (1992) 373; W. Schülke, A. Kaprolat, T. Fischer, K. Höppner and F. Wohlert, *Rev. Sci. Instrum.* **66** (1995) 2446

[84] M. Ito and Y. Amemiya, *Nucl. Instr. and Meth. A* **310** (1991) 369

[85] P. Suortti and T. Tschentscher, *Rev. Sci. Instrum.* **66** (1995) 1798; P. Suortti, T. Buslaps, P. Fajardo, V. Honkimäki, M. Kretzschmer, U. Lienert, J. E. McCarthy, M. Renier, A. Shukla, T. Tschentscher and T. Meinander, *J. Synchr. Rad.* **6** (1999) 69

[86] P. Suortti, P. Pattison and W. Weyrich, *J. Appl. Cryst.* **19** (1986) 336; *ibid.* 343

[87] U. Lienert, Ph.D. Thesis: *Scattering of High Energy X-Rays*, University of Manchester, UK (1995)

[88] Certified Systems, USA

[89] W. A. Caliebe, Ph.D. Thesis: *Inelastic X-Ray Scattering with High Energy Resolution*, Christian-Albrechts Universität zu Kiel, Germany (1997)

[90] The X21A3 is a Phase-II design for beamline X21. The original Phase-I design (X21A1) is still operational. For a description on X21A1, see: C.-C. Kao, K. Hämäläinen, M. Krisch, D. P. Siddons, T. Oversluizen and J. B. Hastings, *Rev. Sci. Instrum.* **66** (1995) 1699

[91] N. Shiotani, N. Sakai, F. Itoh, M. Sakurai, H. Kawata, Y. Amemiya and M. Ando, *Nucl. Instr. and Meth. A* **275** (1989) 447; F. Itoh, M. Sakurai, T. Sugawa, K. Suzuki, N. Sakai, M. Ito, O. Mao, N. Shiotani, Y. Tanaka, Y. Sakurai, S. Nanao, H. Kawata, Y. Amemiya and M. Ando, *Rev. Sci. Instrum.* **60** (1989) 2402

[92] Y. Sakurai, M. Ito, T. Urai, Y. Tanaka, N. Sakai, T. Iwazumi, H. Kawata, M. Ando and N. Shiotani, *Rev. Sci. Instrum.* **63** (1992) 1190

[93] Y. Sakurai, *J. Synchr. Rad.* **5** (1998) 208

[94] R. Verbeni, F. Sette, M. H. Krisch, U. Bergmann, B. Gorges, C. Halcousis, K. Martel, C. Masciovecchio, J. F. Ribous, G. Ruocco and H. Sinn, *J. Synchr. Rad.* **3** (1996) 62

[95] F. Sette, R. Ruocco, M. Krisch, U. Bergmann, C. Masciovecchio, V. Mazzacurati, G. Signorelli and R. Verbeni, *Phys. Rev. Lett.* **75** (1995) 850; F. J. Bermejo, M. Alvarez and S. M. Bennington, *Phys. Rev. Lett.* **76** (1996) 3656;

F. Sette, R. Ruocco, M. Krisch, U. Bergmann, C. Masciovecchio, V. Mazzacurati, G. Signorelli and R. Verbeni, *ibid.* 3657; F. Sette, R. Ruocco, M. Krisch, C. Masciovecchio, R. Verbeni and U. Bergmann, *Phys. Rev. Lett.* **77** (1996) 83

[96] E. Bürkel, B. Dörner, T. Illini and J. Peisl, *J. Appl. Cryst.* **24** (1991) 1042; B. Dörner, E. Bürkel and J. Peisl, *Nucl. Instr. and Meth. A* **426** (1986) 450

[97] M. Schwoerer-Böhning, A. T. Macrander, P. M. Abbamonte and D. A. Arms, *Rev. Sci. Instrum.* **69** (1998) 3109

[98] W. Nakel, *Phys. Rep.* **243** (1994) 317

[99] H. W. Koch and J. W. Motz, *Rev. Mod. Phys.* **31** (1959) 920

[100] R. H. Pratt and I. J. Feng, in *Atomic Inner-Shell Physics*, ed. B. Crasemann, Plenum (1985)

[101] N. G. Alexandropoulos, T. Chatzigeogiou, G. Evangelakis, M. J. Cooper and S. Manninen, *Nucl. Instr. and Meth. A* **271** (1988) 543

[102] S. Manninen and T. Paakkari, *Phys. Rev. B* **44** (1991) 2928

[103] A. Andrejczuk, L. Dobrzyński, J. Kwiatkowska, F. Maniawski, S. Kaprzyk, A. Bansil, E. Żukowski and M. J. Cooper, *Phys. Rev. B* **48** (1993) 15552

[104] B. K. Sharma, *Z. Naturforsch.* **48A** (1993) 334 U. Mittal, B. K. Sharma and R. K. Kothari, *ibid.* 348; B. K. Sharma, B. L. Ahuja, U. Mittal, S. Perkkiö, T. Paakkari and S. Manninen, *Pramana* **46** (1996) 289

[105] B. K. Sharma, B. L. Ahuja, U. Mittal, S. Perkkiö, T. Paakkari and S. Manninen, *Pramana* **46** (1996) 289

[106] A. Andrejczuk, E. Żukowski, L. Dobrzyński and M. J. Cooper, *Nucl. Instr. and Meth. A* **337** (1993) 133

[107] G. Basavaraju, P. P. Kane and S. M. George, *Phys. Rev. A* **36** (1987) 655

[108] S. M. Lad, G. Basavaraju and P. P. Kane, *Phys. Rev. A* **42** (1990) 1267

[109] R. H. Pratt, C. D. Shaffer, N. B. Avdonina, X.-M. Tong and V. Florescu *Nucl. Instr. and Meth. B* **99** (1995) 156; C. D. Shaffer, Xiao-Min Tong and R. H. Pratt, *Phys. Rev. A* **53** (1996) 4158; R. H. Pratt, *Indian J. Phys. B* **71** (1997) 349

[110] W. A. Reed and P. Eisenberger, *Phys. Rev. B* **6** (1972) 4596

[111] S. Manninen, T. Paakkari and K. Kajantie, *Phil. Mag.* **29** (1974) 167

[112] V. Halonen, *Report Series in Physics* **D 3** (1975), University of Helsinki, Finland; B. G. Williams and V. Halonen, *Physica Fennica* **10** (1975) 5; V. Halonen, B. G. Williams and T. Paakkari, *ibid.* 107; V. Halonen and B. G. Williams, *Acta Cryst. A* **31** (1975) S229; P. Paatero and V. Halonen, *Nucl. Instr. and Meth.* **135** (1976) 537; V. Halonen and B. G. Williams, *Phys. Rev. B* **19** (1979) 1990; R. Serimaa, T. Pitkänen, S. Vahvaselkä and T. Paakkari, *J. Appl. Cryst.* **23** (1990) 11

[113] J. Felsteiner, P. Pattison and M. J. Cooper *Phil. Mag.* **30** (1974) 537

[114] J. Felsteiner and W. Schülke, *Nucl. Instr. and Meth. B* **132** (1997) 1

[115] P. Fajardo, V. Honkimäki, T. Buslaps and P. Suortti, *Nucl. Instr. and Meth. B* **134** (1998) 337

[116] S. Manninen and T. Paakkari, *Nucl. Instr. and Meth.* **155** (1978) 115; R. S. Holt, J. L. DuBard, M. J. Cooper, T. Paakkari and S. Manninen, *Phil. Mag. B* **39** (1979) 541

[117] D. A. Cardwell and M. J. Cooper, *Phil. Mag. B* **54** (1986) 37

[118] D. L. Anastassopoulos, and G. D. Priftis, N. I. Papanicolaou, N. C. Bacalis and D. A. Papaconstantopoulos, *J. Phys.: Condens. Matter* **3** (1991) 1099; D. L. Anastassopoulos and G. D. Priftis, *Nucl. Instr. and Meth. A* **314** (1992) 504

[119] S. Manninen and P. Suortti, *Phil. Mag. B* **40** (1979) 199

[120] S. Manninen, M. J. Cooper and D. A. Cardwell, *Nucl. Instr. and Meth. A* **245** (1986) 485

[121] A. J. Rollason, J. Felsteiner, G. E. W. Bauer and J. R. Schneider, *Nucl. Instr. and Meth. A* **256** (1987) 532

[122] S. Manninen, *Phys. Rev. Lett.* **57** (1986) 1500; K. Namikawa and S. Hosoya, *ibid.* 1501

[123] M. J. Cooper, *Radiat. Phys. Chem.* **50** (1997) 63

[124] P. M. Berstrom and R. H. Pratt, *Radiat. Phys. Chem.* **50** (1997) 3

[125] Y. Takada, *Phys. Rev. B* **43** (1991) 5962; Y. Takada and H. Yasuhara, *Phys. Rev. B* **44** (1991) 7879

[126] S. Manninen, K. Hämäläinen, T. Paakkari and P. Suortti, *J. Phys. (Paris) Colloq.* **48** (1987) C9-823

[127] Z. Kaliman, T. Surić, K. Pisk and R. H. Pratt, *Phys. Rev. A* **57** (1998) 2683

[128] K. Hämäläinen, *Nucl. Instr. and Meth. A* **297** (1990) 521; K. Hämäläinen, S. Manninen and J. R. Schneider, *ibid.* 526

[129] *Intermetallic Compounds*, Volumes 1 & 2, edited by J. H. Westbrook and R. L. Fleischer, Wiley (1995)

[130] P. Chaddah and V. C. Sahni, *Phil. Mag. B* **37** (1978) 305; S. Manninen, B. K. Sharma, T. Paakkari, S. Rundqvist and M. W. Richardsson, *Phys. Status Solidi B* **107** (1981) 749

[131] R. Podloucky and A. Neckel, *Phys. Status Solidi B* **95** (1979) 541

[132] S. Manninen, V. Honkimäki and P. Suortti, *J. Appl. Cryst.* **25** (1992) 268

[133] C. Blaas, J. Redinger, S. Manninen, V. Honkimäki, K. Hämäläinen and P. Suortti, *Phys. Rev. Lett.* **75** (1995) 1984

[134] C. Sternemann, G. Döring, C. Wittkop, W. Schülke, A. Shukla, T. Buslaps and P. Suortti, *J. Phys. Chem. Solids* **61** (2000) 379; K. J. Chen, V. Caspar, C. Bellin and G. Loupias, *Solid State Comm.* **7** (1999) 357

[135] W. Schülke, G. Stutz, F. Wohlert and A. Kaprolat, *Phys. Rev. B* **54** (1996) 14381

[136] E. Daniel and S. H. Vosko, *Phys. Rev.* **120** (1960) 2041

[137] B. Brandow, *Phys. Rep.* **296** (1998) 1

[138] E. Dagotto, *Rev. Mod. Phys.* **66** (1994) 763; E. Dagotto, *J. Phys. Chem. Solids* **59** (1998) 1699

[139] H. Ushio and H. Kamimura, *J. Phys. Soc. Jpn.* **64** (1995) 2585; A. Sano, M. Eto and H. Kamimura, *Int. J. Mod. Phys. B* **32** (1997) 3733; A. Sano, Y. Suwa and H. Kamimura, *ibid.* 3751; H. Ushio and H. Kamimura, *ibid.* 3759; H. Ushio and H. Kamimura, *ibid.* 3797; S. Matsuno, H. Ushio, Y. Suwa and H. Kamimura, *ibid.* 3815; H. Kamimura, K. Nomura and A. Sano, *J. Phys.: Condens. Matter* **10** (1998) 11345

[140] H. Fukuyama, *J. Phys. Chem. Solids* **59** (1998) 447; V. J. Emery and S. A. Kivelson, *J. Phys. Chem. Solids* **59** (1998) 1705

[141] J. G. Naeini, X. K. Chen, J. C. Irwin, M. Okuya, T. Kimura and K. Kishio, *Phys. Rev. B* **59** (1999) 9642

[142] A. L. Wachs, P. E. A. Turchi, Y. C. Jean, K. H. Wetzler, R. H. Howell, M. J. Fluss, D. R. Harshmann, J. P. Remeika, A. S. Cooper and R. M. Fleming, *Phys. Rev. B* **38** (1988) 913; P. E. A. Turchi, A. L. Wachs, Y. C. Jean, R. H. Howell, K. H. Wetzler and M. J. Fluss, *Physica C* **153-5** (1988) 157; P. E. A. Turchi, A. L. Wachs, K. H. Wetzler, J. H. Kaiser, R. N. West, Y. C. Jean, R. H. Howell and M. J. Fluss, *J. Phys.: Condens. Matter* **2** (1990) 1635; P. A. Sterne, R. H. Howell, M. J. Fluss, J. H. Kaiser, K. Kitazawa and H. Kojima, *J. Phys. Chem. Solids* **54** (1993) 1231; R. H. Howell, P. A. Sterne, M. J. Fluss, J. H. Kaiser, K. Kitazawa and H. Kojima, *Phys. Rev. B* **49** (1994) 13127

[143] J.-H. Guo, N. Wassdahl, P. Skytt, S. Butorin, Y. Ma and J. Nordgren, *J. Phys. Chem. Solids* **54** (1993) 1203; J.-H. Guo, S. M. Butorin, N. Wassdahl, P. Skytt, J. Nordgren and Y. Ma, *Phys. Rev. B* **49** (1994) 1376

[144] D. A. Fischer, A. R. Moodenbaugh and Y. Xu, *Physica C* **215** (1993) 279

[145] C. T. Chen, L. H. Tjeng, J. Kwo, H. L. Kao, P. Rudolf, F. Sette and R. M. Fleming, *Phys. Rev. Lett.* **68** (1992) 2543; E. Pellegrin, N. Nücker, J. Fink, S. L. Molodtsov, M. Gutiérrez, E. Navas, O. Strebel, Z. Hu, M. Domke, G. Kaindl, S. Uchida, Y. Nakamura, J. Markl, M. Klauda, G. Saemann-Ischenko, A. Krol, J. L. Peng, Z. Y. Li and R. L. Greene, *Phys. Rev. B* **47** (1993) 3354

[146] J. C. Fuggle, P. J. W. Weijs, R. Schoorl, G. A. Sawatsky, J. Fink, N. Nücker, P. J. Durham and W. M. Temmermann, *Phys. Rev. B* **37** (1988) 123; N. Nücker, J. Fink, J. C. Fuggle, P. J. Durham and W. M. Temmermann, *Phys. Rev. B* **37** (1988) 5158; N. Nücker, H. Romberg, X. X. Xi, J. Fink, G. Gegenheimer and Z. X. Zhao, *Phys. Rev. B* **39** (1989) 6619; H. Romberg, M. Alexander, N. Nücker, P. Adelmann and J. Fink, *Phys. Rev. B* **42** (1990) 8768

[147] P. Day, M. Rosseinsky, K. Prassides, W. I. F. David, O. Moze and A. Soper, *J. Phys. C: Solid State Phys.* **20** (1987) L429

[148] H. A. Blackstead and J. D. Dow, *J. Appl. Phys.* **78** (1995) 7175; H. A. Blackstead and J. D. Dow, *J. Appl. Phys.* **81** (1997) 6285

[149] S. Kaprzyk and A. Bansil, *Phys. Rev. B* **42** (1990) 7358; A. Bansil and S. Kaprzyk, *Phys. Rev. B* **43** (1991) 10335; A. Bansil, S. Kaprzyk and J. Tobola, in *Application of Multiple Scattering Theory to Materials Science*, edited by W. H. Butler *etal.*, MRS Symposia Proceedings No. 253, Materials Research Society, Pittsburgh, USA (1992)

[150] U. von Barth and L. Hedin, *J. Phys. C* **5** (1972) 1629

[151] G. Lehmann and M. Taut, *Phys. Status Solidi B* **54** (1972) 469

[152] L. Lam and P. M. Platzman, *Phys. Rev. B* **9** (1974) 5122

[153] A. Soyer, Laboratoire de Minéralogie-Cristallographie associé au CNRS, Universités P. et M. Curie et D. Diderot, Paris, France, *http://www.iucr.org/sincris-top/logiciel/laueX/en/laueX_en.html*

[154] A. Shukla, B. Barbiellini, A. Erb, A. Manuel, T. Buslaps, V. Honkimäki and P. Suortti, *Phys. Rev. B* **59** (1999) 12127; S. Manninen, K. Hämäläinen, M. A. G. Dixon, M. J. Cooper, D. A. Cardwell and T. Buslaps, *Physica C* **314** (1999) 19

[155] A. Yamamoto, *Acta Cryst. A* **52** (1996) 509; A. Cervellino, T. Haibach and W. Steurer, *Phys. Rev. B* **57** (1998) 11223; T. Janssen, J. L. Birman, V. A. Koptsik, M. Senechal, D. Weigel, A. Yamamoto, S. C. Abrahams and T. Hahn, *Acta Cryst. A* **55** (1999) 761

[156] S. J. Poon, *Adv. in Phys.* **41** (1992) 303

[157] S. Ranganathan, K. Chattopadhyay, A. Singh and K. F. Kelton, *Progr. Mat. Sci.* **41** (1997) 195

[158] T. Fujiwara and H. Tsunetsugu, *Electronic Structure and Transport of Quasicrystals*; A. E. Carlsson and R. Phillips, *Electronic-Structure and Total-Energy Calculations for Quasicrystals and Related Crystals*; both in *Quasicrystals: The State of the Art*, edited by D. P. DiVicenzo and P. Steinhardt, World Scientific (1991)

[159] G.T. de Laissardiere and T. Fujiwara, *Phys. Rev. B* **50** (1994) 9843; R. F. Sabiryanov, S.K. Bose, and S.E. Burkov, *J. Phys.: Condens. Matter* **7** (1995) 5437;

[160] M. Honal, T. Haibach and W. Steurer, *Acta Cryst. A* **54** (1998) 374; W. Steurer and T. Haibach, *Acta Cryst. A* **55** (1999) 48

[161] M. Krajčí, J. Hafner and M. Mihalkovič, *Phys. Rev. B* **55** (1997) 843; M. Krajčí, J. Hafner and M. Mihalkovič, *Phys. Rev. B* **56** (1997) 3072; M. Krajčí and J. Hafner, *Phys. Rev. B* **58** (1998) 5378

[162] J. L. Wagner, B. D. Biggs and S. J. Poon, *Phys. Rev. Lett.* **65** (1990) 203; W. Yun-Ping, Z. Dian-Lin and L. F. Chen, *Phys. Rev. B* **48** (1993) 10542

[163] S. Lin, X. Wang, L. Lu, D. Zhang, L. X. He and K. X. Kuo, *Phys. Rev. B* **41** (1990) 9625; D. N. Basov, T. Timusk, F. Barakat, J. Greedan and B. Grushko, *Phys. Rev. Lett.* **72** (1994) 1937; K. Edagawa, M. A. Chernikov, A. D. Bianchi, E. Felder, U. Gubler and H. R. Ott, *Phys. Rev. Lett.* **77** (1996)

1071; L. Shuyuan, L. Guohong and Z. Dian-Lin, *ibid.* 1998; A. D. Bianchi, F. Bommeli, E. Felder, M. Kenzelman, M. A. Chernikov, L. Degiorgi, H. R. Ott and K. Edagawa, *Phys. Rev. B* **58** (1998) 3046

[164] W. Steurer, T. Haibach, B. Zhang, S. Kek and R. Lück, *Acta Cryst. B* **49** (1993) 661

[165] Y. Tanaka, Y. Sakurai, S. Nanao, N. Shiotani, M. Ito, N. Sakai, H. Kawata and T. Iwazumi, *J. Phys. Soc. Jpn.* **63** (1994) 3349

[166] Y. Nanao, T. Shibuya, S. Takeuchi, W. Liu, X.-S. Li and S. Berko, *Phys. Rev. B* **46** (1992) 3108;

[167] Y. Tanaka, S. Nanao and S. Tanigawa, *J. Phys.: Condens. Matter* **9** (1997) 11247

[168] F. Dugain, M. de Boissieu, K. Shibata, R. Currat, T. J. Sato, A. R. Kortan, J.-B. Suck, K. Hradil, F. Frey and A. P. Tsai, *Eur. Phys. J. B* **7** (1999) 513

[169] A. P. Smith and N. W. Ashcroft, *Phys. Rev. Lett.* **59** (1987) 1365; J. Friedel, *Helv. Phys. Acta*, **61** (1988) 538; S. E. Burkov, T. Timusk and N. W. Ashcroft *J. Phys.: Condens. Matter* **4** (1992) 9447; S. E. Burkov, A. A. Varlamov and D. V. Livanov, *Phys. Rev. B* **53** (1996) 11504

[170] G. W. Zhang, Z. M. Stadnik, A.-P. Tsai and A. Inoue, *Phys. Rev. B* **50** (1994) 6696; X. Wu, S. W. Kycia, C. G.Olson, P. J. Benning, A. I. Goldman and D. W. Lynch, *Phys. Rev. Lett.* **75** (1995) 4540; D. N. Davydov, D. Mayou, C. Berger, C. Gignoux, A. Neumann, A. G. M. Jansen and P. Wyder, *Phys. Rev. Lett.* **77** (1996) 3173; Z. M. Stadnik, D. Purdie,M. Garnier, Y. Baer, A.-P. Tsai, A. Inoue, K. Edagawa and S. Takeuchi, *ibid.* 1777

[171] Z. M. Stadnik, G. W. Zhang, A.-P. Tsai and A. Inoue, *Phys. Rev. B* **51** (1995) 11358; Z. M. Stadnik, D. Purdie, M. Garnier, Y. Baer, A.-P. Tsai, A. Inoue, K. Edagawa, S. Takeuchi and K. H. J. Buschow, *Phys. Rev. B* **55** (1997) 10938

[172] I. R. Fisher, M. J. Kramer, Z. Islam, A. R. Ross, A. Kracher, T. Wiener, M. J. Sailer, A. I. Goldman and P. C. Canfield, *Phil. Mag. B* **79** (1999) 425